University
of Dundee

University of Dundee

Bed load sediment transport and morphological evolution in a degrading uniform sediment channel under unsteady flow hydrographs

Wang, Le; Cuthbertson, Alan; Pender, Gareth; Zhong, Deyu

Bed Load Sediment Transport and Morphological Evolution in a Degrading Uniform Sediment Channel Under Unsteady Flow Hydrographs

Le Wang[1,2] (ID), Alan Cuthbertson[3] (ID), Gareth Pender[4] (ID), and Deyu Zhong[1] (ID)

[1]State Key Laboratory of Hydroscience and Engineering, Tsinghua University, Beijing, China, [2]School of Civil and Hydraulic Engineering, Ningxia University, Yinchuan, China, [3]School of Science and Engineering (Civil Engineering), University of Dundee, Dundee, UK, [4]School of Energy, Geoscience, Infrastructure and Society, Heriot Watt University, Edinburgh, UK

Abstract Flume experiments are conducted to investigate the intrinsic links between time-varying bed load transport properties for uniform sediments and bed surface morphology under unsteady hydrograph flows, in the absence of upstream sediment supply. These conditions are representative of regulated river reaches (e.g., downstream of a dam) that are subject to natural flood discharges or managed water releases, resulting in net degradation of the river bed. The results demonstrate that the hydrograph magnitude and unsteadiness have significant impacts on sediment transport rates and yields, as well as hysteresis patterns and yield ratios generated during the rising and falling limbs. A new hydrograph descriptor combining the influence of total water work and unsteadiness on bed load transport is shown to delineate these hysteresis patterns and yield ratios while correlating strongly with overall sediment yields. This provides an important parametric link between unsteady hydrograph flow conditions, bed load transport, and bed surface degradation under imposed zero sediment feed conditions. As such, maximum bed erosion depths and the longitudinal bed degradation profiles along the flume are strongly dependent on the magnitude of this new hydrograph descriptor. Similarly, nonequilibrium bedforms generated along the flume indicate that formative conditions for alternate bars, mixed bar/dunes, or dunes are defined reasonably well by an existing morphological model and the new hydrograph descriptor. These findings provide a new framework for improved predictive capabilities for sediment transport and morphodynamic response in regulated rivers to natural or imposed unsteady flows, while their wider application to graded sediments is also considered.

1. Introduction

In natural fluvial systems, sediment transport is linked intrinsically to the prevalent unsteady hydraulic conditions within the river channel and the upstream supply of sediments, with the occurrence of the bulk sediment transport typically concentrated during flood events (Berta & Bianco, 2010; Phillips & Sutherland, 1990). Ongoing statistical data collection by the Dartmouth Flood Observatory (Brakenridge, 2016) indicates that the number of extreme flood events is increasing worldwide due to climate change, implying that natural rivers globally are likely to experience more dramatic changes to bulk sediment transport and channel bed morphology in the future. Furthermore, within regulated rivers where the supply of sediments is often controlled by the presence of a dam, an increase in extreme flood events has the potential to increase net degradation in the downstream channel either from the passage of higher-magnitude flood events or the increased frequency of managed flow releases. It is therefore essential to expand our current understanding of sediment transport and morphological changes within regulated river systems in response to the passage of flood events to implement more appropriate management strategies for water and sediment resources and, thus, mitigate socioeconomic impacts associated with increasing flood and erosion risk. Current knowledge of flow-sediment-morphology interactions remains relatively poorly understood, especially as direct measurements of sediment transport in natural gravel bed rivers during periods of high flood flow are relatively sparse and extremely difficult to obtain (Graf & Qu, 2004; Mao, 2012; Mao et al., 2010). As such, appropriately scaled, well-controlled laboratory experiments remain an essential tool to improving fundamental understanding of complex processes and interdependencies that occur in regulated river channels under limited or controlled upstream sediment supply.

To date, most experimental studies investigating sediment transport processes in unsteady flows have modeled hydrographs that (1) consist of incrementally increasing and decreasing steady-state flow steps (i.e.,

stepped hydrographs; Waters & Curran, 2015; Martin & Jerolmack, 2013; Parker et al., 2007; Piedra, 2010), (2) have short overall event durations lasting from several seconds to several minutes (i.e., flood waves; Bombar et al., 2011; Graf & Qu, 2004; Pathirana et al., 2006), (3) apply constant flow accelerations and decelerations during the rising and falling limbs (i.e., triangular- or trapezoidal-shaped hydrographs; Bombar et al., 2011; Wong & Parker, 2006), or (4) consider a limited range of unsteady flow conditions, with no systematic investigation of hydrograph characteristics on the sediment transport response (Humphries et al., 2012; Mao, 2012; Parker et al., 2007). Despite the availability of several nondimensional parameters to help characterize unsteady flow, such as hydrograph *unsteadiness* (Graf & Suszka, 1985) and *total water work* (Yen & Lee, 1995), the influence of these key parameters on bed load sediment transport properties such as hysteretic effects has not, as yet, been studied systematically over a wide range of flow conditions. For example, Hassan et al. (2006) simulated the effects on gravel bed armoring processes of stepped hydrographs with different magnitudes and durations, finding that sediment transport was always higher during the rising limb (i.e., clockwise [CW] hysteresis). This effect was attributed more to the limitation in upstream sediment supply rather than the hydrograph characteristics. By contrast, Lee et al. (2004) observed counterclockwise (CCW) hysteresis under similar no sediment supply conditions, an effect they attributed to the temporal lag of bedform evolution compared to changes in the unsteady flow conditions. Their results also highlighted that increased flow unsteadiness generally resulted in larger bed load yields, following a general power law relationship. Bombar et al. (2011) also observed CCW hysteresis for triangular or trapezoidal hydrographs under no sediment supply, finding that normalized bed load yields decreased exponentially and increased linearly with increasing flow unsteadiness and total water work, respectively. In flow-sediment recirculating flume studies, Mao (2012) found that CW hysteresis patterns became more evident in response to lower-magnitude hydrographs. This effect was attributed to changes in the organizational structure of surface sediments affecting entrainment and, hence, bed load transport before and after the peak flow. Waters and Curran (2015) also conducted flow-sediment recirculating experiments with stepped low- and high-magnitude asymmetric hydrograph sequences over graded sand-silt and sand-gravel sediment beds. Their findings suggested that transport hysteresis patterns varied due to bedform and surface structure adjustments, as well the stabilizing effects from antecedent flow. Overall, their measured bed load yields were found to increase as both unsteadiness and total water work increased.

These previous studies present variable, and often contradictory, findings in relation to sediment transport properties and the evolution of bed morphology that can be attributed to imposed experimental conditions relating to (i) bed composition (i.e., uniform or graded sediments), (ii) upstream sediment supply (i.e., recirculating or zero feed), and (iii) unsteady flow characteristics. A common feature of all these studies is that the hydrograph unsteadiness and total water work were not varied systematically and independently to determine their individual and combined effects on bed load transport rates, hysteresis patterns, and total sediment yields, as well as on associated morphological changes.

Much of the fundamental knowledge of bedform development (e.g., ripples, dunes, and bars) has been derived from equilibrium studies conducted under steady flow conditions with continuous sediment supplies (Carling, 1999; Raudkivi, 1997; Yalin, 1992). Direct evidence of morphodynamic evolution and nonequilibrium bedforms developed under the unsteady flows and sediment supply-limited boundary conditions remains, by comparison, relatively sparse (Allen, 2009; Church, 2006; Wijbenga & Klaassent, 2009). This knowledge gap is particularly relevant to regulated rivers where net bed degradation and associated morphology will be influenced strongly by the limited upstream sediment supply and the availability of in-channel stored bed sediments. The present paper reports findings from flume experiments that investigate systematically the influence of design hydrograph flow parameters on both bed load sediment transport and bed surface evolution under zero sediment supply imposed at the upstream boundary. In this sense, our results are analogous to flow-sediment-morphology scenarios likely to be encountered in river reaches immediately downstream of a dam or reservoir.

2. Scaling Considerations

2.1. Unsteady Flow Hydrographs

To describe quantitatively the rate of change in flow conditions during the passage of a flow hydrograph, a nondimensional *unsteadiness* parameter Γ_{HG} was introduced by Graf and Suszka (1985) and Suszka (1987)

as a function of the ratio between the change in flow depth $\Delta H = H_p - H_b$ (i.e., between the base H_b and peak H_p flow depths) and the total hydrograph duration $\Delta T = \Delta T_R + \Delta T_F$ (i.e., the sum of rising and falling limb durations), such that

$$\Gamma_{\text{HG}} = \frac{1}{u_b^*} \frac{\Delta H}{\Delta T}, \tag{1}$$

where u_b^* is the reference shear velocity (m/s) for the base flow condition. Clearly, if Γ_{HG} is large, the hydrograph will be flashy in nature, corresponding to the passage of a flood wave, while lower Γ_{HG} values approaching 0 correspond to a mildly unsteady flow approaching equivalent steady flow conditions. As well as this unsteadiness, the overall magnitude of a flow hydrograph can be represented by the total water volume V_{ol} discharged over its duration, corresponding to the area under the unsteady part of the hydrograph. A nondimensional parameter known as the *total water work* W_k has been defined previously (Bombar et al., 2011; Lee et al., 2004; Yen & Lee, 1995) to quantify this magnitude, as follows:

$$W_k = \frac{u_b^{*2} V_{\text{ol}}}{g H_b^3 B}, \tag{2}$$

where B is the channel width (m), V_{ol} is the total water volume under the unsteady hydrograph (m^3), H_b is the initial base flow depth (m), and g is the gravitational acceleration (m/s^2). It is also anticipated that hydrograph shape may have an important role in determining bed load transport properties and changes to channel morphology. Asymmetrical hydrographs are often generated in rivers from rainfall-derived flood events with shorter rising limb ΔT_R and longer receding limb ΔT_F durations. However, other types of events, such as glacial outburst flows (i.e., jökulhlaup; Rushmer, 2007) or controlled water releases from dams, may have the opposite asymmetry. In the context of the current study, the influence of asymmetry is considered through the time ratio η of rising to falling limb durations, as follows:

$$\eta = \frac{\Delta T_R}{\Delta T_F}. \tag{3}$$

Hydrographs with $\eta = 1$ are, by definition, symmetrical, while $\eta > 1$ and $\eta < 1$ represent unsymmetrical hydrographs with longer rising and falling limb durations, respectively. In the context of hydrograph unsteadiness Γ_{HG} (equation (1)), the effect of η is independent assuming the overall depth change ΔH and hydrograph duration ΔT remain unchanged (De Sutter et al., 2001).

Dynamic similitude between the experiment and fluvial scales is ensured by matching the Froude numbers of prevalent flow conditions. For all experimental flow conditions, the base flow remained fixed (see section 3.2), with maximum peak flows up to $Q_p = 0.058$ m^3/s; $H_p = 0.120$ m (Table 1). The corresponding Froude numbers in the experiments ranged from $Fr = 0.52$–0.59 (i.e., subcritical). With a length scale factor $\lambda_L = 1/20$ assumed between the flume and river channel, corresponding river flow depths $H = 1.14$–2.40 m and the equivalent time scale factor $\lambda_T = (1/20)^{1/2} = 0.224$. Therefore, the experimental hydrograph durations $\Delta T = 900$–$36,000$ s (see Table S1 in supporting information) correspond to equivalent river hydrograph durations of $\Delta T \approx 1.1$–44.6 hr. This can therefore be considered to cover a wide range of natural flood events or managed dam releases, with relatively mild to high (i.e., flashy) unsteadiness.

2.2. Bed Load Sediment Transport

Nondimensional parameterizations are also required to describe the sediment bed response to unsteady flow conditions, with bed load transport rates commonly described by the normalized bed load parameter (Einstein, 1942), which, for uniform sediments, is given by

$$q_b^* = \frac{q_b}{\rho_s \sqrt{\left(\frac{\rho_s}{\rho} - 1\right) g d_{50}^3}}, \tag{4}$$

where q_b is bed load transport rate (kg·m^{-1}·s^{-1}), ρ_s and ρ are density of sediment and fluid, respectively, and d_{50} is the (median) sediment grain size. Similarly, the total sediment mass flux transported during the unsteady flow hydrograph can be represented by the normalized total bed load yield W_t^* (e.g., Bombar et al., 2011), such that

Table 1
Design Hydrograph Parameters and Corresponding Bed Load Transport Properties

Group	Run no.	Q_p (L/s)	H_p (m)	Γ_{HG} (×10^{-4})	W_k	η	ξ	$q_{b,\max}$ (g·m^{-1}·s^{-1})	W_t (kg)	W_t^* (×10^4)	ψ	Hysteresis pattern[a]
	U1a (V1a, S1a)	58	0.120	1.389	234.3	1	39.7	88.8	205.93	5.523	1.16	CW
S1	S1b	58	0.120	1.389	231.5	0.4	39.2	114.3	194.98	5.230	0.94	CW
	S1c	58	0.120	1.389	231.5	2.5	39.2	86.0	183.08	4.910	1.72	CW
U1	U1b	50	0.110	0.929	226.1	1	35.3	58.1	163.46	4.384	1.14	CW
	U1c	45	0.103	0.674	233.8	1	34.2	47.2	156.30	4.192	1.49	CW
	U1d	41	0.098	0.507	233.6	1	32.3	43.3	162.08	4.347	1.32	CW
	U1e	34	0.087	0.263	231.6	1	28.1	25.8	129.69	3.479	1.15	CW
V1	V1b	50	0.110	1.467	143.6	1	24.6	70.2	119.76	3.212	1.19	CW
	V1c	40	0.096	1.577	68.5	1	11.9	43.0	51.44	1.380	1.04	M/N
	V1d	35	0.089	1.657	41.3	1	7.25	30.1	31.45	0.844	1.22	M/N
	V1e	28	0.078	1.776	15.3	1	2.71	24.5	11.35	0.304	1.02	M/N
	U2a (V2a)	58	0.120	2.778	117.2	1	22.8	94.9	106.72	2.862	1.03	M/N
U2	U2b	38	0.093	0.789	117.2	1	17.7	34.8	82.99	2.226	1.30	M/N
	U2c	28	0.078	0.237	117.5	1	14.0	17.1	65.79	1.765	1.21	M/N
V2	V2b	40	0.096	3.154	34.2	1	6.83	39.7	26.89	0.721	1.15	M/N
	V2c	28	0.078	3.553	7.6	1	1.56	14.5	4.50	0.121	0.58	CCW
	U3a (V3a)	58	0.120	5.555	58.6	1	13.1	107.6	60.25	1.616	1.00	M/N
U3	U3b	38	0.093	1.579	58.6	1	10.2	42.3	45.30	1.215	1.11	M/N
	U3c	28	0.078	0.474	58.7	1	8.02	17.8	34.45	0.924	1.25	M/N
V3	V3b	40	0.096	6.308	17.1	1	3.92	49.5	15.48	0.415	0.63	CCW
	V3c	28	0.078	7.105	3.8	1	0.89	26.6	3.82	0.103	0.45	CCW

Note. The highlighted cells indicate the benchmark design hydrograph runs (U$_{1a}$, U$_{2a}$, and U$_{3a}$) and the variables that are varied systematically in each experimental group (e.g., S$_1$, U$_1$, and V$_1$). CW = clockwise; CCW = counterclockwise; M/N = mixed/no.
[a]Represents the hysteresis for bed-load transport rates measured over the duration of each hydrograph.

$$W_t^* = \frac{W_t}{\rho_s b d_{50}^2}. \tag{5}$$

W_t is the total bed load mass transport (kg) collected in a sediment trap over the hydrograph duration, and b is the sediment trap width (=0.37 m, i.e., less than channel width B). This sediment yield parameter W_t^* provides information on the bulk transport response over the full hydrograph duration, while the specific influence of Γ_{HG}, W_k and η on transport yields attained during the rising and falling hydrograph limbs can be defined by the sediment yield ratio ψ, as follows:

$$\psi = \frac{W_{t,r}^*}{W_{t,f}^*}, \tag{6}$$

where $W_{t,r}^*$ and $W_{t,f}^*$ represent the nondimensional transport yields (equation (5)) measured separately during the rising and falling hydrograph limbs, respectively.

2.3. Channel Degradation and Bed Morphology

A combined theoretical-experimental study by Tubino (1991) indicated that the ratio of characteristic time scales associated with unsteady flow conditions and morphological adjustment at the bed surface affects both the instantaneous growth rate and phase of bar perturbations, as well as controlling the amplitude of the final equilibrium bedform configuration. The current study represents the first time that Tubino's theoretical model has been applied to interpret bedform development under zero sediment supply boundary conditions. It is therefore anticipated that discrepancies between this theoretical approach and experimental measurements may arise from changes in the availability of in-channel stored sediments over the duration of the unsteady hydrograph flows tested. As such, the final bed surface morphology will be quantified in terms of both (i) the micro (i.e., ripple) → macro (i.e., bar) bedforms generated and (ii) the longitudinal
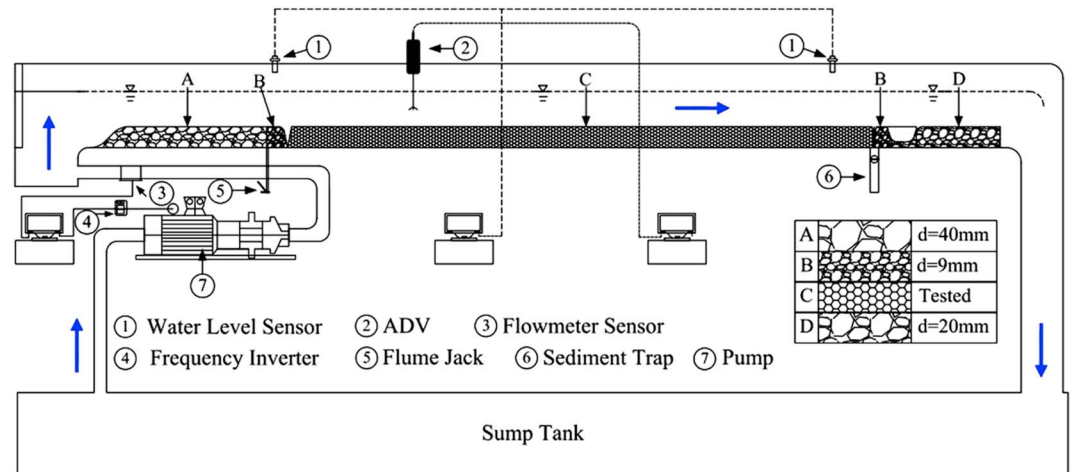
Figure 1. Schematic representation of flume and experimental setup.

bed surface profiles generated through depletion of in-channel stored sediments. This combined analysis provides important new insight into the morphodynamic response of regulated rivers to flood hydrograph events and/or managed releases generated under sediment supply-limited conditions.

3. Experimental Program

3.1. Flume Setup and Bed Sediments

The experimental studies were performed in a 22-m-long, 0.75-m-wide, and 0.5-m-deep flow recirculating, tilting flume channel (see Figure 1). The variable flow rate was controlled by a programmable pump frequency inverter capable of producing smooth, continuous hydrographs (where flow rates Q vary continually with time) of any desired shape, with peak flow rates up to 100 L/s. These unsteady flows were measured continuously in the pipe delivering water to the channel using a nonintrusive ultrasonic flow meter. Uncertainty associated with the pump performance and flow measurement accuracy (± 0.01 L/s) resulted in minor differences between the flow delivery to the channel and prescribed design flows (see section 3.3). (Note: statistical analysis indicated an average discrepancy of 0.002 L/s [i.e., average relative error = 0.003–0.012% over range of unsteady flows tested], while the maximum variability due to instantaneous flow fluctuations was estimated as ± 0.28 L/s [i.e., maximum relative error = 0.48–1.65%]).

The initial 5-m inlet section and 3-m downstream section of the flume bed were artificially roughened with coarse open-work gravel ($d_{50} = 40$ and 20 mm, respectively, labeled A and D in Figure 1) to (i) ensure a fully developed turbulent boundary layer was established prior to the erodible test bed section, (ii) prevent excessive scour at the channel inlet, and (iii) catch any sediments transported beyond the sediment trap (Figure 1). The central 14-m-long test bed section (labeled C in Figure 1) was covered by an 11-cm-thick layer of quasi-uniform, coarse sand (i.e., $d_{50} = 1.95$ mm; $\gamma_s = 2.65$) that was screeded flat to match the mean surface elevation of the upstream and downstream immobile gravel bed sections. No additional sediment was supplied at the upstream end of the flume during the experiments in order to simulate the zero feed conditions.

3.2. Experimental Procedure

All experimental runs were conducted at an initial longitudinal bed slope S_0 of 0.002 and were initiated with a steady, uniform base flow rate $Q_b = 17.0$ L/s and depth $H_b = 0.058$ m, designed to satisfy near-threshold conditions based on the critical Shields stress parameter $\tau_{br}^* \approx 0.042$ for the sand bed layer (see section (S1) of supporting information for details on base flow conditions, Shields threshold and shear velocity calculations). The corresponding reference bed shear velocity for this base flow condition $u_b^* \approx (g.H_b.S_0)^{1/2} = 0.034$ m/s was used to calculate Γ_{HG} and W_k parameters via equations (1) and (2), respectively and was maintained along the channel for a relatively short period of 15 min to rework and stabilize the sediment bed layer prior to the onset of the design flow hydrographs. During the base flow period, transverse bed elevation profiles to a lateral spatial resolution of 5 mm were obtained using a downlooking acoustic Doppler velocimetry

probe (with a measurement accuracy of ± 0.1 mm) at 0.25-m intervals along the full length of the sand test bed to generate an initial bed surface elevation map. Statistical analysis of these surface maps indicated that the standard deviation of spatially varying bed elevations was $\sigma_z = 0.84$ mm, significantly smaller than the median grain size ($d_{50} = 1.95$ mm) of the coarse sand grade used in the experiments.

Temporal variations in the inflow rates and water surface elevations were measured synchronously throughout the duration of each hydrograph by the ultrasonic flow meter in the supply pipe and ultrasonic level sensors located at the channel inlet and outlet (Figure 1). Bed load sediment transport rates were measured directly from samples collected in the sediment trap located toward the downstream end of the sand bed section. The sampling time intervals were varied between 2.5 and 30 min for different test runs according to the sediment transport intensity and the overall hydrograph duration (see Table S1 in the supporting information). At the end of each run, with base flow conditions reestablished in the channel, a final bed surface elevation map was obtained at the same lateral resolution and longitudinal positions as before, allowing changes in bed surface morphology associated with bed degradation and the development of bedforms to be investigated.

3.3. Design Flow Hydrographs

Seven groups of design flow hydrographs were tested (see Table S1 and Figure S1 in section (S2) of supporting information) within which hydrograph asymmetry η (group S1), total water work W_k (groups V1–V3), or unsteadiness Γ_{HG} (groups U1–U3) were varied systematically with respect to benchmark hydrographs (highlighted in Table S1). Within each experimental grouping, the individual influence on bed load sediment transport and bed surface morphology from the hydraulic parameter under consideration was tested by keeping all other parameters largely constant. This was achieved by adjusting peak flows Q_p and hydrograph durations ΔT between runs to vary W_k and Γ_{HG} (Groups V1–V3 and U1–U3, respectively, Table S1), and the duration of rising ΔT_R and receding ΔT_F limbs to vary η for fixed Q_p and ΔT values (Group S1, Table S1). The majority of hydrographs were symmetrical (i.e., $\eta = 1$). This was deemed the most appropriate shape to determine systematically the effects of W_k and Γ_{HG} on sediment transport rates, hysteresis patterns and bed load yields, as the flow rate of change dQ/dt was, by definition, symmetrical during the rising and receding limbs.

4. Results

4.1. Sediment Transport Properties

Bed load sediment transport properties including peak transport rates $q_{b,\mathrm{max}}$, dimensional W_t and nondimensional W_t^* sediment yields (equation (5)), sediment yield ratios ψ (equation (6)), and transport hysteresis patterns are summarized in Table 1 for all hydrograph flow conditions tested.

4.1.1. Bed Load Transport Rates

Example plots of bed load transport rates q_b generated over different hydrographs are presented in Figure 2. All plots from groups S1, U1, and V1 (Table 1) showing the individual effects of η, Γ_{HG}, and W_k, respectively, are provided in the supporting information (Figure S2 and section (S3)). As expected, bed load transport rates q_b generally increase and decrease during the rising and falling hydrograph limbs, respectively, with peak transport rates $q_{b,\mathrm{max}}$ occurring close to the peak flow Q_p. The specific influence of hydrograph asymmetry η indicates that the largest peak transport rate ($q_{b,\mathrm{max}} = 114.3$ g·m^{-1}·s^{-1}; run S1b, Table 1) occurs under the hydrograph with the shorter rising limb (i.e., $\eta = 0.4$, Figure 2b) and, hence, the highest rate of increase in flow dQ/dt. The individual influences of hydrograph unsteadiness and total water work indicate a more systematic reduction in peak transport rates when either Γ_{HG} decreases (i.e., $q_{b,\mathrm{max}} = 58.1 \rightarrow 25.8$ g·m^{-1}·s^{-1}; runs U1b $\rightarrow$ U1e, Table 1) or W_k decreases (i.e., $q_{b,\mathrm{max}} = 70.2 \rightarrow 24.5$ g·m^{-1}·s^{-1}; runs V1b $\rightarrow$ V1e, Table 1). Both effects are as expected due to attenuation associated with (i) flatter, less unsteady hydrographs (i.e., reduced Q_p values over longer durations $\rightarrow$ lower Γ_{HG} and fixed W_k values, Figure 2c), or (ii) lower-magnitude hydrographs (i.e., reduced Q_p values over shorter durations $\rightarrow$ lower W_k and fixed Γ_{HG} values, Figure 2d). The influence of Γ_{HG} is also demonstrated by comparing peak transport rates for benchmark hydrographs with equivalent Q_p values but reducing durations (i.e., runs U1a $\rightarrow$ U2a $\rightarrow$ U3a, Table 1). This shows that although W_k reduces between these hydrographs, the corresponding increase in Γ_{HG} results in higher $q_{b,\mathrm{max}}$ values (i.e., $q_{b,\mathrm{max}} = 88.8 \rightarrow 94.9 \rightarrow 107.6$ g·m^{-1}·s^{-1}, Table 1). This again indicates that larger
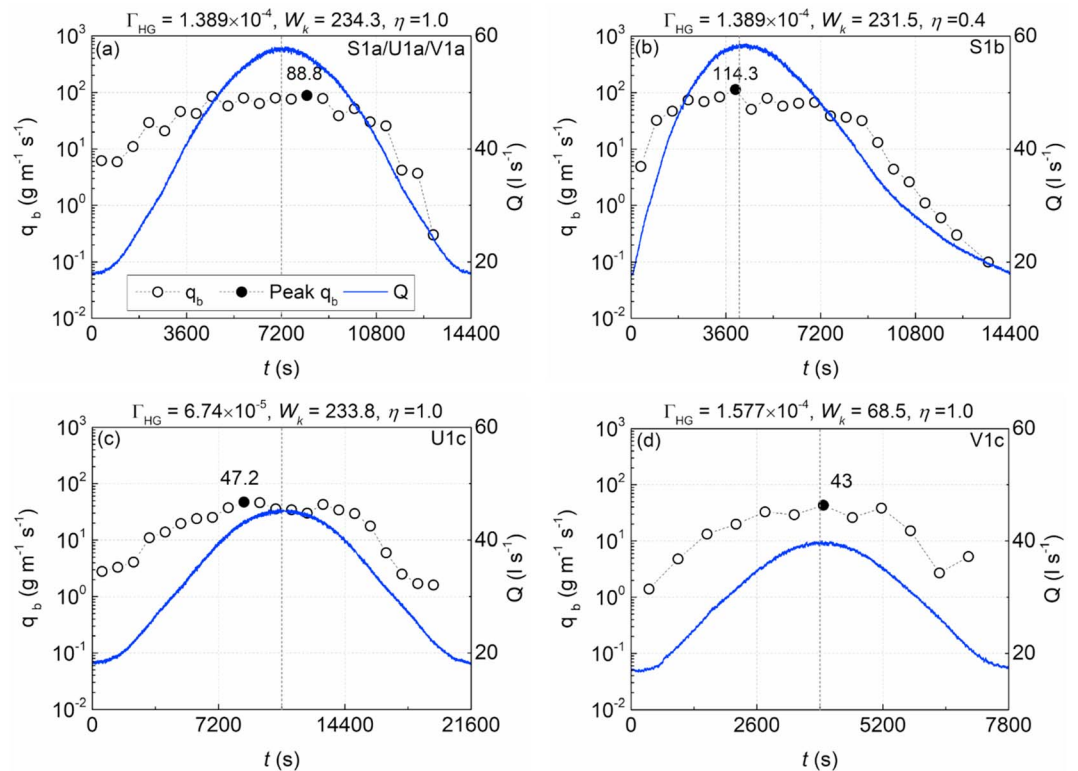
Figure 2. Example plots showing temporal variation in flow Q and bed load transport q_b rates for runs (a) S1a (U1a, V1a), (b) S1b, (c) U1c, and (d) V1c (see Table 1).

dQ/dt values during the rising limb, associated with higher Γ_{HG} values, increases peak transport rates and is thus consistent with the η-varying hydrograph with the shortest rising limb duration (Figure 2b).

It is also apparent that measured q_b values often indicate a degree of plateauing (i.e., $dq_b/dt \approx 0$) in the hydrograph region prior to and after the peak flow Q_p. This is particularly evident in hydrographs with higher Q_p values, under which more intensive bed load transport typically occurs (see Figure 2). A consequence of this plateauing effect, as well as the discrete time intervals over which individual q_b measurements were obtained, is that no consistent temporal lag is observed between peak flow Q_p and peak transport $q_{b,\max}$, unlike in a number of previous studies (e.g., Bombar et al., 2011; Graf & Qu, 2004; Lee et al., 2004).

4.1.2. Bed Load Hysteresis

Direct phase plots of q_b versus Q are used to classify the bed load transport hysteresis for the range of hydrographs tested. Example phase plots are presented in Figure 3 for the same runs as shown in Figure 2 (note: all phase plots for groups S1, U1, and V1 are provided in supporting information Figure S3 and section S3, while hysteresis patterns for all runs are given in Table 1). Overall, the majority of runs exhibit CW or mixed/no (M/N) bed load hysteresis, with only three runs displaying CCW hysteresis. For the η-varying hydrographs (group S1, Table 1), the q_b: Q phase plots (Figures 3a and 3b) indicate CW hysteresis over the majority of the hydrograph duration, except in the peak flow region where differences between q_b values at equivalent flow rates on the rising and falling limbs diminish. This is consistent with the bed load plateauing observed around the peak flow region of some hydrographs (Figure 2) and is in accordance with findings from Humphries et al. (2012) and Mao (2012). The specific influence of Γ_{HG} indicates that, while CW hysteresis patterns remain throughout group U1 (Figures 3a and 3c and Table 1), the difference between q_b values at equivalent Q values on the rising and falling limbs tends to reduce with Γ_{HG} (see Figures S3d–S3g). This may result from the combination of reduced q_b values and longer bed load sampling durations for runs with lower Γ_{HG} values (i.e., runs U1b → U1e, Table S1). For groups U2 and U3, the corresponding hysteresis patterns are consistently M/N (Table 1), suggesting that W_k (and not Γ_{HG}) may have a greater influence on bed load hysteresis. Indeed, comparing Figure 3a ($W_k = 234.3$) and Figure 3d ($W_k = 68.5$) suggests a transition
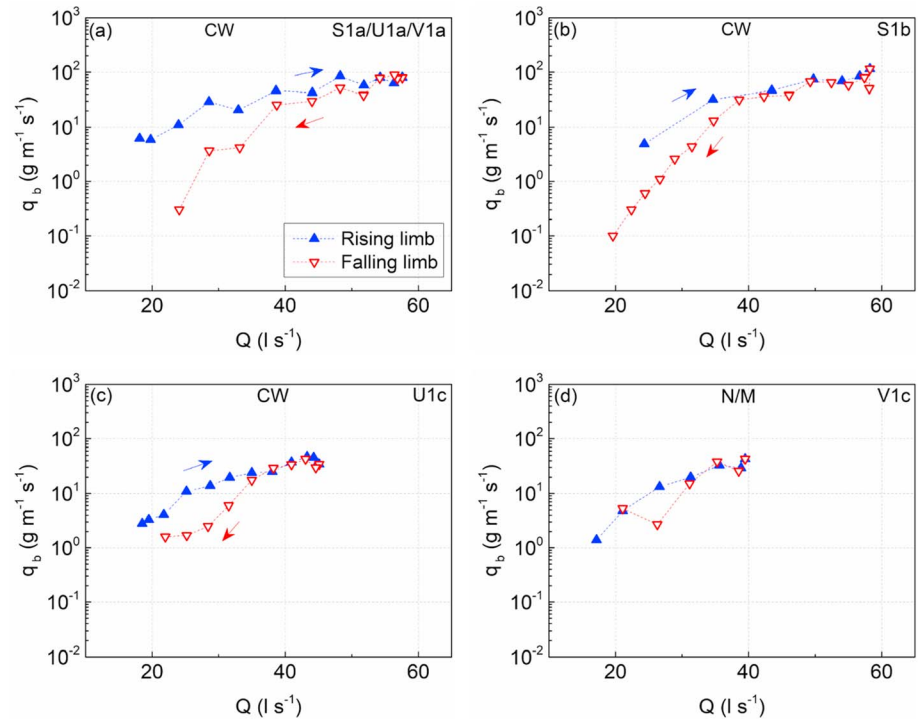
Figure 3. Example plots of bed load hysteresis patterns for runs (a) S1a (U1a, V1a), (b) S1b, (c) U1c, and (d) V1c (see Table 1). CW = clockwise, N/M = no/mixed.

from CW to M/N hysteresis occurs under similar Γ_{HG} values within group V1 (Table 1 and Figures S3h–S3k), while a similar transition from M/N to CCW hysteresis occurs within groups V2 ($W_k = 117.2 \rightarrow 7.6$) and V3 ($W_k = 58.6 \rightarrow 3.8$; see Table 1).

4.1.3. Sediment Yields

The individual influences of η, Γ_{HG}, and W_k on normalized bed load yields W_t^* (equation (5)) over the duration of each hydrograph and yield ratios ψ (equation (6)) between the rising and receding limbs are analyzed in this section, with these quantities summarized in Table 1 for all hydrographs tested in the seven experimental groups. First, the influence of hydrograph asymmetry (group S1, Table 1) on W_t^* appears to be minimal, with values remaining largely constant at the three η values tested. It is also acknowledged that while this finding is based on a very limited number of runs, it is consistent with previous results presented in Wang et al. (2015) and Phillips et al. (2018). It is also an interesting result given that $q_{b,\mathrm{max}}$ values vary with η (see Figures 2a and 2b and Table 1) but indicates clearly that W_k and Γ_{HG} are expected to have a greater influence on the overall sediment yields generated. Intuitively, larger sediment yields are expected during higher magnitude hydrograph events, and a strong correlation is demonstrated between W_k and W_t^* for all runs in the current study (Figure 4a) that satisfies the following power law relationship:

$$W_t^* = 229.93 W_k^{0.9705}, \left(R^2 = 0.979\right). \tag{7}$$

Similar regression analysis of equivalent data from Lee et al. (2004) (also plotted on Figure 4a) indicates a comparable power law relationship: $W_t^* = 260.59\, W_k^{0.9291}$ ($R^2 = 0.959$). By contrast, equivalent correlation between Γ_{HG} and W_t^* (Figure 4b) does not collapse to a single regression curve. Here, the different experimental groupings in which Γ_{HG} is varied systematically (i.e., U1–U3, Table 1) are separated depending on the corresponding magnitude of W_k within these groups. Each individual data set plotted in Figure 4b (including runs U1A-6 from Lee et al., 2004) show a monotonic increase in W_t^* with Γ_{HG}, indicating that shorter, steeper hydrographs transport more sediment over their duration than longer, flatter events with equivalent W_k values. This finding is also in accord with the reduction in $q_{b,\mathrm{max}}$ values observed for hydrographs with decreasing Γ_{HG} values (Figures 2a and 2c and Table 1).
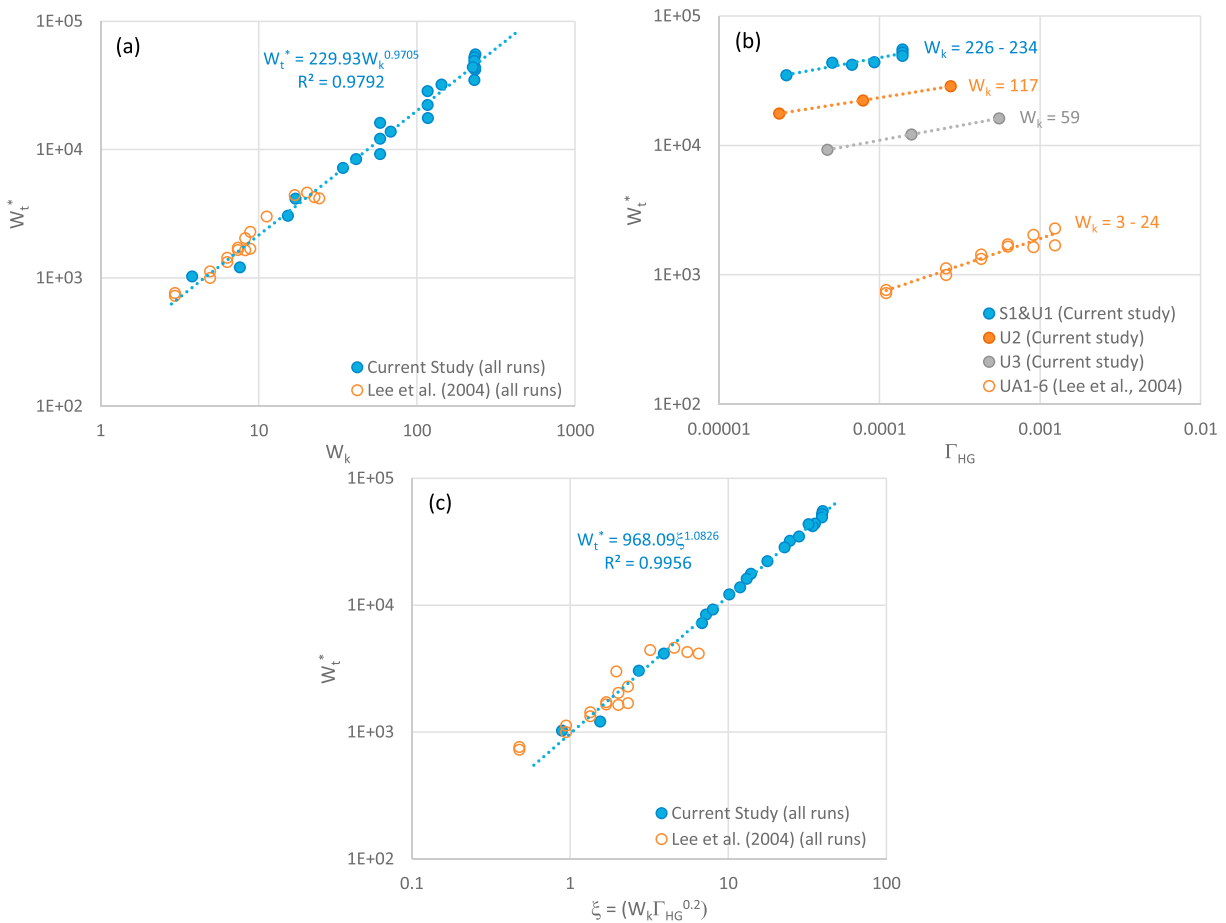
Figure 4. Variation of bed load yield W_t^* with (a) total water work W_k (all runs, Table 1), (b) unsteadiness Γ_{HG} (groups U1–U3) and (c) $\xi = W_k\,\Gamma_{HG}^{0.2}$ (all runs). Data from Lee et al. (2004) plotted for comparative purposes.

Further regression analysis on our data is used to develop a combined hydrograph parameter ξ that accounts for the relative influence of W_k and Γ_{HG} on measured sediment yields, similar to Waters and Curran (2015) analysis (see section 5.1.3). In our case, the most appropriate form of this parameter is $\xi = W_k\,\Gamma_{HG}^{\alpha}$, where exponent $\alpha = 0.2$ provides the best overall correlation ($R^2 > 0.99$) to the measured W_t^* values (Figure 4c), following the power law relationship:

$$W_t^* = 968.09\xi^{1.0826}, \quad \left(R^2 = 0.996\right). \tag{8}$$

This new combined hydrograph parameter ξ and its relationship with W_t^* also demonstrates good overall agreement with the equivalent uniform sediment data of Lee et al. (2004) (plotted in Figure 4c for comparative purposes). Further discussion of the general applicability of combined hydrograph descriptors to uniform and graded bed load sediment transport generated under unsteady hydrograph flows is provided in section 5.1.3.

4.1.4. Bed Load Yield Ratio

The proportion of the total bed load yield transported during the rising and falling hydrograph limbs provides a useful quantitative indicator of the impact that imposed zero sediment feed conditions have on the relative availability of in-channel stored sediments over the duration of each run. This quantity is expressed directly as the bed load yield ratio ψ (equation (6)) in Table 1 and is expected to be closely related to bed load hysteresis patterns discussed previously (section 4.1.2). For the η-varying hydrographs (group S1, Table 1), ψ values are clearly influenced by the relative duration of the rising and falling limbs, increasing from $\psi = 0.94$ to 1.72 as η increases from 0.4 to 2.5. Given that the overall sediment yield W_t^* remains largely unchanged by η (Table 1), the range of ψ values is clearly in accord with the CW transport hysteresis observed in the η-
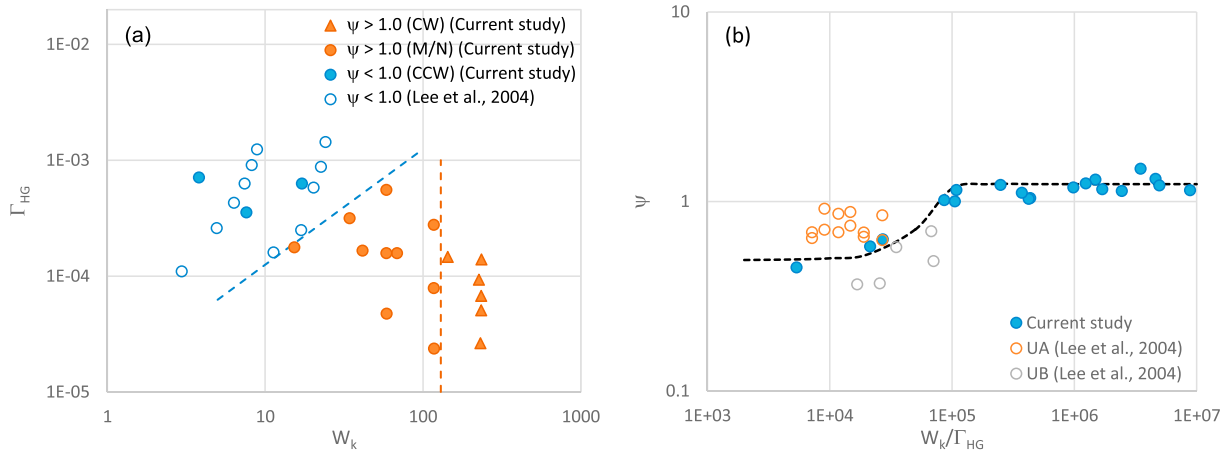
Figure 5. (a) Regime plot of bed load yield ratios $\psi < 1$ and $\psi > 1$ in Γ_{HG}: W_k space, and (b) variation of ψ with W_k/Γ_{HG}. Data from Lee et al. (2004) plotted for comparative purposes.

varying hydrographs (see Figures 3a and 3b and Table 1), especially when the relative limb durations ΔT_R and ΔT_F are taken into account through η.

A regime plot of ψ values obtained from all symmetrical ($\eta = 1$) hydrographs is presented in Γ_{HG}: W_k space in Figure 5a, along with comparative data from Lee et al. (2004). This plot indicates a clear distinction between the regions where $\psi \geq 1$ (i.e., higher W_k and lower Γ_{HG} values) and $\psi < 1$ (i.e., higher Γ_{HG} and lower W_k values), which coincide directly to the runs displaying CW (or M/N) and CCW transport hysteresis, respectively (see Table 1). Additionally, the $\psi \geq 1$ data indicate a further division at $W_k \approx 130$ between runs displaying CW and M/N hysteresis patterns. As with transport hysteresis (section 4.1.2), the overall prevalence of runs with $\psi \geq 1$ suggests that changes to the bed surface morphology (i.e., net bed degradation and bedform development) resulting from the imposed zero sediment feed may reduce progressively the availability of in-channel stored sediments and alter prevalent unsteady flow conditions over the hydrograph duration. It is noted that the range of $\psi \geq 1$ values attained (i.e., up to $\psi = 1.49$ for run U1c, Table 1) does not indicate that in-channel sediment supplies are exhausted completely during any of the hydrographs tested (discussed in section 4.2.1 in relation to final bed elevation profiles). By contrast, the three flow hydrographs conditions under which $\psi < 1$ and CCW hysteresis were observed (Table 1), along with the comparative data from Lee et al. (2004), may be more indicative of inertial effects influencing the temporal lag in sediment transport properties and bedform development during the rising and falling hydrograph limbs (Oh & Tsai, 2010). Finally, hydrographs with $\psi \approx 1$ and/or M/N hysteresis patterns appear to be closer to the idealized conditions adopted in conventional bed load sediment transport equations that take no account of potential differences in transport rates and yields during rising and falling limbs.

The general trend for runs with $\psi \geq 1$ and $\psi < 1$ in the Γ_{HG}: W_k regime plot indicates that this transition between these two regions occurs at $W_k/\Gamma_{HG} \approx 8 \times 10^4$ (i.e., gradient of blue dashed line, Figure 5a) As such, ψ values from the current study and Lee et al. (2004) can be plotted against W_k/Γ_{HG} (Figure 5b) to determine the relative importance of both hydrograph parameters. As expected, the plot shows that $\psi < 1$ when $W_k/\Gamma_{HG} < \sim 8 \times 10^4$ (i.e., hydrographs with lower magnitude and/or higher unsteadiness) and $\psi \geq 1$ when $W_k/\Gamma_{HG} > \sim 8 \times 10^4$ (i.e., higher magnitude and/or lower unsteadiness). It is important to note that the $\psi \geq 1$ data do not increase systematically with W_k/Γ_{HG}, suggesting the impact of in-channel sediment depletion on ψ remains largely consistent between these runs. Overall, the observed relationship between ψ and W_k/Γ_{HG} is relatively well represented by a Boltzmann-type function, producing the sigmoidal curve shown in Figure 5b ($R^2 = 0.87$), of the form:

$$\psi = P_1 + \frac{P_2 - P_1}{1 + \exp\left(\frac{W_k/\Gamma_{HG} - 62,567}{15,847}\right)}. \tag{9}$$

Here, coefficients $P_1 = 1.234$ and $P_2 = 0.474$ are clearly valid for symmetrical hydrographs over the range $10^3 \leq W_k/\Gamma_{HG} \leq 10^7$ considered in the current study, while the equivalent data from Lee et al. (2004) are also

shown to reside on either side of this trend line within the $\psi < 1$ region. The form of this Boltzmann-type relationship indicates a relatively abrupt transition ($W_k/\Gamma_{HG} = 10^4 \rightarrow 10^5$) between $\psi = 0.5 \rightarrow 1.2$, implying that bed load transport is generally asymmetric ($\psi \neq 1$) for net degrading sediment beds generated under zero feed conditions. This is again attributed to (i) sediment transport inertia during the rising limb (for lower W_k/Γ_{HG} values) and (ii) in-channel sediment depletion during the falling limb (for higher W_k/Γ_{HG} values). The general validity of equation (9) over a wider range of hydrograph conditions remains unclear for the following reasons: (i) only three data points are obtained within the $\psi < 1$ region (with no repetition of runs and significant scatter observed in equivalent data from Lee et al., 2004); (ii) as $W_k/\Gamma_{HG} \rightarrow 0$, the total water work diminishes and/or the unsteadiness increases resulting in greater bed load inertial effects during the rising limb with $\psi \rightarrow 0$; and (iii) as $W_k/\Gamma_{HG} \rightarrow \infty$, the total water work increases and/or unsteadiness diminishes (i.e., equivalent to a quasi-steady flow), resulting in exhaustion of available in-channel sediments during the elongated rising limb and $\psi \rightarrow \infty$.

4.2. Bed Morphology
4.2.1. Bed Elevation Changes
In the absence of an upstream sediment supply, it is apparent that the bed load yields generated by individual flow hydrograph events must arise exclusively from the net erosion and degradation of in-channel stored sediments within the test bed section (Figure 1). Direct comparison of initial and final width-averaged, longitudinal bed elevation profiles obtained from the measured bed surface maps can therefore determine the magnitude and nature of channel bed incision observed over the range of hydrographs tested. Example plots of these width-averaged bed elevation profiles are shown in Figures 6a–6c for specific hydrograph events tested in groups S1, U1, and V1 (see Table 1). In the majority of runs, net bed degradation is observed along the full length of the test section, with the largest incision depths Δz_0 typically occurring at the upstream end of the test section (i.e., $x = 0$), reducing progressively along the channel. The slope of the final degraded bed surface also adjusts asymptotically to the initial bed slope with increasing downstream distance, with localized fluctuations in these profiles indicative of the development of bedforms (see section 4.2.2). For η-varying hydrographs (Figure 6a), the longitudinal profiles reveal slightly lower incision depths for asymmetrical hydrographs ($\eta = 0.4$ and 2.5; runs S1b and S1c), commensurate with the marginally lower bed load yields W_t^* attained in these runs (Table 1). Similarly, Figures 6b and 6c indicate a general, but consistent, reduction in incision depths along the channel as both Γ_{HG} and W_k decrease, again in accord with corresponding reductions in W_t^* values (Figures 4a–4c and Table 1). For hydrographs with low W_k values, bed degradation diminishes along the channel and a net deposition region forms immediately downstream of the initial bed incision zone (run V1e, Figure 6c). This may arise due to (i) reduced bed load transport carrying capacities at low W_k values and (ii) disparity between timescales associated with the unsteady flow and morphological adjustment. With the well-defined relationship between W_t^* and combined hydrograph parameter ξ established previously (equation (8)), the normalized initial channel incision depth $\Delta z_0^* = \Delta z_0/H_b$ (where H_b is the base flow depth) is shown to correlate well with ξ (Figure 6d), following a similar power law relationship:

$$\Delta z_0^* = 0.2191\xi^{0.4944}, \left(R^2 = 0.976\right). \tag{10}$$

The overall asymptotic adjustment in nondimensional bed degradation profiles $\Delta z^*(x^*)/\Delta z_0^*$ along the length of the test bed section $x^* = x/L$ is found to be well represented by a general exponential function, with empirical coefficients dependent on the combined hydrograph parameter ξ and fitted through regression analysis (see section (S4) in the supporting information for details).

4.2.2. Bedform Development
Detailed bed elevation maps were obtained over the erodible test bed section (Figure 1), prior to and immediately following the passage of each flow hydrograph, to determine the spatial variation in bed deformations $\Delta z(x,y) = z(x,y) - z_0(x,y)$ (i.e., variance from the initially flat bed condition $z_0(x,y)$) due to net erosion ($\Delta z < 0$) and deposition ($\Delta z > 0$). Typical bed elevation surface maps for a range of hydrographs (i.e., runs U1a, U1c, U1e, and V1d; Table 1) are plotted in Figure 7. These plots consider only the bed section downstream of the initial, deeper channel incision region (i.e., $x \geq 3$ m) and, thus, highlight distinctive spatial variations in Δz revealing the nature and geometry of different bedforms developing under the different flow hydrographs (detailed for all runs in Table 2). Figures 7a and 7b show two test conditions under which
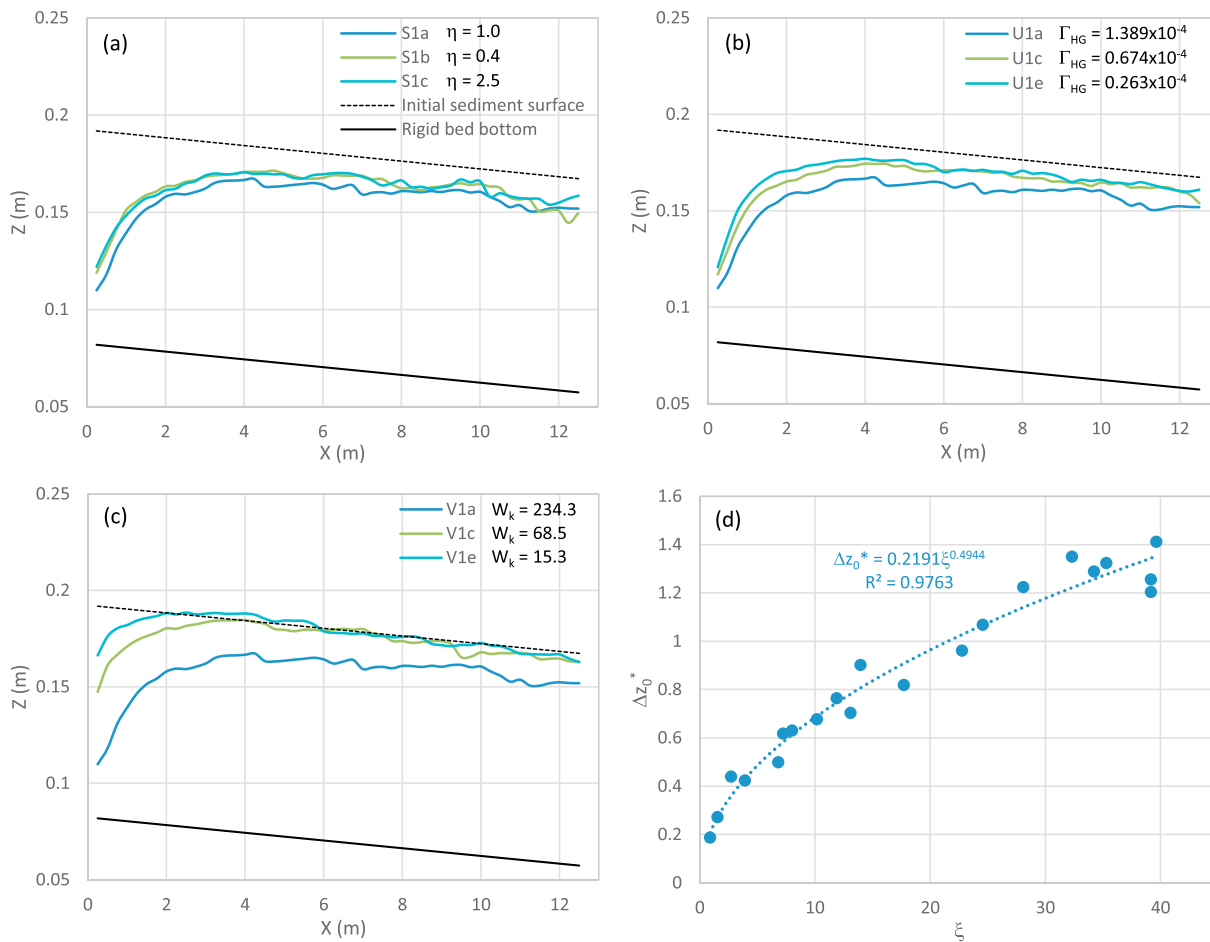
Figure 6. (a–c) Width-averaged bed elevation profiles showing influence η, Γ_{HG} and W_k, (d) variation in normalized initial channel incision depth Δz_0^* with ξ.

distinctive alternate bars patterns (indicated by red and blue arrows) form under net degradational bed conditions (i.e., Δz up to -30 and -20 mm, respectively). These, and the other runs in which alternate bars are observed, occur under hydrographs with the largest ξ values (i.e., $\xi \geq 34$, Table 2). By contrast, other hydrographs that generate less well defined bar structures (e.g., Figure 7c), or combinations of bars and dunes, correspond typically to an intermediate range of ξ values (i.e., ~13 $\leq \xi \leq$ ~32, Table 2). Finally, test runs in which more regular dunes form (e.g., Figure 7d), within beds indicating both localized aggregation (Δz up to $+5$ mm) and degradation (Δz up to -15 mm), correspond to hydrographs with the lowest ξ values (i.e., ~1 $\leq \xi \leq$ ~12). This demonstrates that well-defined, large-scale alternate bars are generated solely for hydrographs with high ξ values that generate the highest sediment yields (i.e., equation (8)) and bed degradation (i.e., equation (10)). By contrast, mixed bars and/or regular dunes are more typically generated under hydrographs with lower ξ values, corresponding to lower W_t^* and Δz_0^* values. This ξ dependence of bedform type is consistent with previous findings from Lee et al. (2004), where regular dunes were found to develop under relatively low values of ξ (i.e., ~0.5 $\leq \xi \leq$ ~6.5, see Table 2).

5. Discussion

5.1. Sediment Transport Response to Hydrograph Flows and Zero Sediment Supply

5.1.1. Variability in Dimensionless Sediment Transport Rates

The observed temporal variability in bed load sediment transport in response to flow hydrographs and zero sediment supply at the upstream boundary is characterized by differential transport rates, hysteresis patterns, and bed load yields during the rising and falling limbs under a wide range of hydrograph
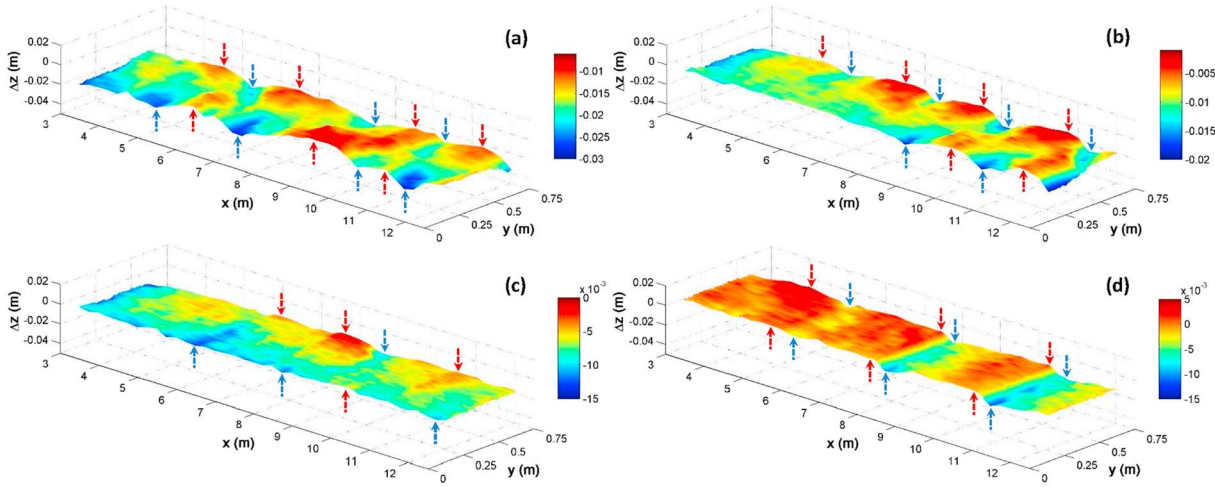
Figure 7. Final bed surface maps showing elevation changes $z(x,y)$ in test bed section for runs (a) U1a (V1a, S1a), (b) U1c, (c) U1e, and (d) V1d (Tables 1 and 2). Red arrows indicate bars/dune crests, while blue arrows indicate pools/dune troughs.

conditions. To account for this variability, Waters and Curran (2015) proposed a modeling approach whereby the bed load transport is predicted separately, under equivalent discharge conditions, on the rising and falling hydrograph limbs. This is obtained through evaluation of a dimensionless transport rate W^*, using the Einstein-Parker dimensionless reference shear stress approach (Parker, 1979; Parker et al., 1982), which can be written for uniform sediments in the general form:

$$W^* = m\left(1 - 0.8351\frac{\tau_{br}^*}{\tau_b^*}\right)^n,$$ (11)

where m and n are modified transport coefficients derived from nonlinear regression and τ_{br}^* is the critical Shields stress, corresponding to the dimensionless reference transport rate $W_r^* = q_b^*/\tau_b^{*3/2} = 0.002$ (e.g., Parker et al., 1982), with q_b^* being the Einstein (1942) bed load parameter (equation (4)). Applying a similar approach here, equation (11) can be fitted to (i) all bed load transport rates measured over the duration of all design hydrographs or (ii) bed load data based on separate measurements during the rising and falling limbs, by deriving bulk and limb-separated τ_{br}^* values, respectively. Run-averaged, dimensionless reference shear stresses were calculated as $\tau_{br}^* = 0.0345$, 0.0336, and 0.0356 for the bulk, rising, and falling limb data sets, respectively, with the resulting plots of W^* versus τ_b^*/τ_{br}^* shown in Figures 8a–8c for these three separate cases. Overall, the data show good general agreement with equation (11) predictions of the bed load transport curve for derived coefficient values $m = 21$ and $n = 2.5$ (i.e., solid black line, Figure 8). Best fit regression trend lines to the data (i.e., dashed lines, Figure 8) also indicate good agreement with equation (11) at higher dimensionless transport rates (i.e., $W^* > 1$) but deviate from the Einstein-Parker relationship at lower W^* values. Regression of the rising limb data has the highest R^2 value (0.86), followed by the bulk ($R^2 = 0.81$) and falling limb ($R^2 = 0.78$) data, reflecting the varying degree to which bed surface morphology, associated with net degradation and bedform development, influences sediment transport properties during the falling limbs of the different hydrograph conditions tested. Grouping bed load data into subsets based on the magnitude of ξ, it is clear for the bulk and rising limb data sets (Figures 8a and 8b, respectively) that there is no obvious influence from ξ on the overall data distribution. However, the falling limb data set (Figure 8c) indicates a general trend where larger W^* values are measured, for the same τ_b^*/τ_{br}^* values, when ξ values are lower. This implies that higher dimensionless transport rates W^* occur during the falling limb when changes to bed morphology, due to net degradation and bedform development, during the rising limb are limited (i.e., under lower ξ values—see Figures 6d and 7).

5.1.2. Variability in Bed Load Transport Hysteresis

It is well recognized that five common classes of hysteresis loop exist for bed load sediment transport under unsteady hydrograph flows, defined as follows: (i) *single-valued*, (ii) *CW*, (iii) *CCW*, (iv) *single-valued plus a loop*, and (v) *figure-8* (e.g., Waters & Curran, 2015; Williams, 1989). A recent review of the different morphological and hydraulic factors affecting hysteresis patterns in sediment transport by Gunsolus and Binns (2017) also indicates that the sediment transport mode, bed composition, sediment supply, hydrograph

Table 2
Details of Bed Form Geometry Generated in Current Study (and Lee et al., 2004) and Parameters for Tubino (1991) Alternate Bar Model (See Section (S5) in the Supporting Information)

Group	Run no.	Γ_{HG} (×10^{-4})	W_k	ξ	σ (= 1/ΔT) (×10^{-4})[a]	$\hat{\sigma}$ (×10^{-4}) (equation (S6))[a]	$\hat{u}$ (equation (S5))[a]	Bed forms	Wavelength λ_{bf} (m)	Height h_{bf} (m)
	U1a (V1a, S1a)	1.389	234.3	39.7	0.694	0.545	2.45	Alternate bars	2.75 ± 0.91	0.017 ± 0.003
S1	S1b	1.389	231.5	39.2	0.694	0.545	2.45	Alternate bars	2.25 ± 0.53	0.023 ± 0.011
	S1c	1.389	231.5	39.2	0.694	0.545	2.45	Alternate bars	1.78 ± 0.65	0.018 ± 0.005
U1	U1b	0.929	226.1	35.3	0.556	0.436	1.96	Alternate bars	3.83 ± 1.51	0.013 ± 0.004
	U1c	0.674	233.8	34.2	0.463	0.363	1.63	Alternate bars	2.55 ± 0.89	0.012 ± 0.004
	U1d	0.507	233.6	32.3	0.397	0.311	1.40	Bars/dunes	2.25 ± 0.43	0.010 ± 0.002
	U1e	0.263	231.6	28.1	0.278	0.218	0.98	Bars/dunes	2.65 ± 0.68	0.008 ± 0.002
V1	V1b	1.467	143.6	24.6	0.877	0.688	3.09	Bars/dunes	—	—
	V1c	1.577	68.5	11.9	1.282	1.01	4.52	Dunes	2.07 ± 0.72	0.010 ± 0.003
	V1d	1.657	41.3	7.25	1.667	1.31	5.88	Dunes	3.00	0.012 ± 0.003
	V1e	1.776	15.3	2.71	2.778	2.18	9.80	Dunes	2.00 ± 0.50	0.009 ± 0.002
	U2a (V2a)	2.778	117.2	22.8	1.389	1.09	4.90	Bars/dunes	3.62	0.023 ± 0.009
U2	U2b	0.789	117.2	17.7	0.694	0.545	2.45	Bars/dunes	2.56 ± 1.52	0.007 ± 0.002
	U2c	0.237	117.5	14.0	0.370	0.291	1.31	Bars/dunes	5.00	0.010
V2	V2b	3.154	34.2	6.83	2.564	2.01	9.04	Dunes	1.50	0.011 ± 0.006
	V2c	3.553	7.6	1.56	5.556	4.36	19.6	Dunes	2.33 ± 0.63	0.008 ± 0.001
	U3a (V3a)	5.555	58.6	13.1	2.778	2.18	9.80	Bars/dunes	1.59 ± 0.48	0.022 ± 0.013
U3	U3b	1.579	58.6	10.2	1.389	1.09	4.90	Dunes	2.00	0.014 ± 0.003
	U3c	0.474	58.7	8.02	0.741	0.581	2.61	Dunes	1.69 ± 0.52	0.007 ± 0.001
V3	V3b	6.308	17.1	3.92	5.128	4.02	18.1	Dunes	1.21 ± 0.49	0.010 ± 0.003
	V3c	7.105	3.8	0.89	11.11	8.72	39.2	Dunes	1.65 ± 0.82	0.009 ± 0.002
Lee et al. (2004)	UA1	1.10	2.96	0.48	3.97	2.48	182.4	Dunes	—	—
	UA2	2.60	4.93	0.95	4.76	2.98	218.9	Dunes	—	—
	UA3	4.30	6.34	1.35	5.56	3.48	255.4	Dunes	—	—
	UA4	6.30	7.40	1.69	6.35	3.98	291.9	Dunes	—	—
	UA5	9.10	8.22	2.03	7.14	4.47	328.3	Dunes	—	—
	UA6	1.24	8.88	2.33	7.94	4.97	364.8	Dunes	—	—
	UB1	1.60	11.27	1.96	2.08	1.30	95.8	Dunes	—	—
	UB2	2.50	16.91	3.22	2.78	1.74	127.7	Dunes	—	—
	UB3	5.80	20.29	4.57	3.47	2.17	159.6	Dunes	—	—
	UB4	8.80	22.54	5.52	4.17	2.61	191.5	Dunes	—	—
	UB5	1.44	24.15	6.53	4.86	3.04	223.5	Dunes	—	—

Note. The highlighted cells indicate the benchmark design hydrograph runs (U_{1a}, U_{2a}, and U_{3a}) and the variables that are varied systematically in each experimental group (e.g., S_1, U_1, and V_1).
[a]See section S5 in the supporting information for details on Tubino (1991) alternate bar model.
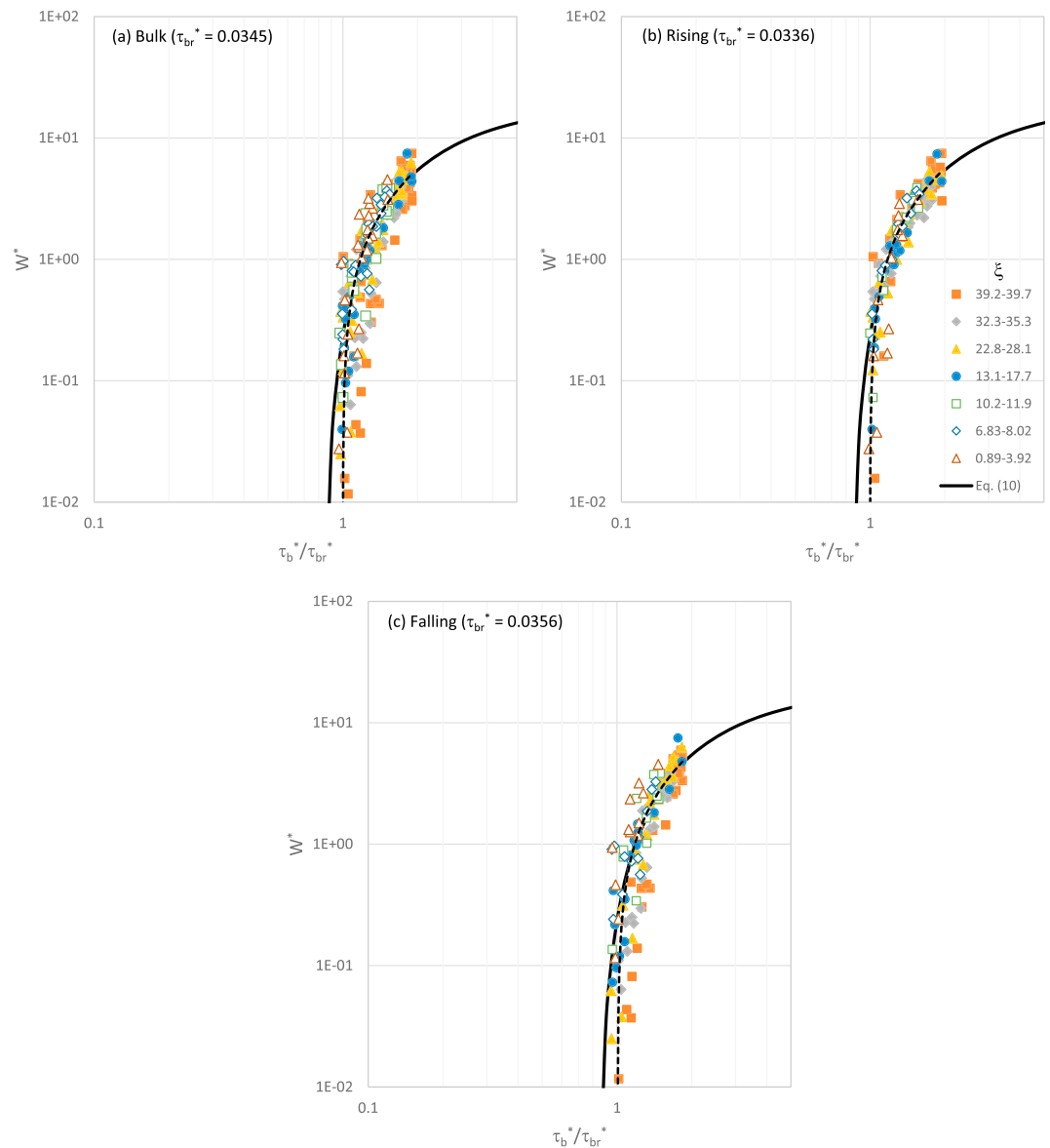
Figure 8. Dimensionless bed load transport rate W^* versus Shields stress ratio τ_b^*/τ_{br}^* for (a) bulk, (b) rising limb, and (c) falling limb data. (Note: fit to equation (11) represented by solid lines, with best fit regression to data also shown as dashed trend lines).

characteristics, and bed morphology all have prominent roles in the type of hysteresis observed. In the current study, the hysteresis patterns for uniform sediment transport under all hydrographs tested are grouped into the three general classifications of CW (i.e., (ii)), CCW (i.e., (iii)), and mixed/no hysteresis (M/N; i.e., (i), (iv), and (v); see Figure 3 and S3). Well-defined CW or CCW hysteresis patterns are shown to correspond universally to runs where the bed load yield ratios $\psi > 1.0$ and $\psi < 1.0$, respectively, although the number of runs displaying $\psi < 1.0$ and CCW hysteresis is very limited (Table 1). In addition, not all runs with $\psi > 1.0$ generate a CW hysteresis, and instead display M/N hysteresis (Figure 5a and Table 1). Considering the direct influence of the combined hydrograph parameter indicates that, in general, CW, M/N and CCW hysteresis occur for hydrographs with the highest (i.e., $\xi = 24.6$–39.7, Table 1), intermediate (i.e., $\xi = 6.83$–22.8), and lowest (i.e., $\xi = 0.89$–3.92) ξ values, respectively. The strong association between large ξ values and CW bed load hysteresis is driven primarily by the large sediment yields (i.e., equation (8)) generated by these hydrographs under zero feed conditions. This has two effects: (i) to reduce the availability of in-channel sediments during the receding hydrograph limb compared to

the rising limb and (ii) to alter unsteady flow conditions during the receding limb due to changes in bed surface morphology associated with progressive bed degradation and the development of large-scale bedforms (see section 4.2). By contrast, CCW hysteresis at lower ξ values appears to result from temporal lag effects between sediment transport, morphological development and the changing unsteady flow conditions (Lee et al., 2004; Waters & Curran, 2015). In this regard, many previous studies (Bombar et al., 2011; Graf & Qu, 2004; Lee et al., 2004) have demonstrated consistently a positive temporal lag exists between peak flow Q_p and peak bed load transport $q_{b,\max}$. This lag is accounted for, at least in part, by the relatively short hydrograph durations tested in these studies, where inertial effects can delay the sediment transport response to rapidly changing flow conditions during the rising limb. Indeed, group V3 runs in current study, with the shortest duration hydrographs (i.e., $\Delta T = 900$–$3{,}600$ s, Table S1), indicate similarly that $q_{b,\max}$ values occur during the receding limb, although the relative bed load sampling frequency may also influence this finding. Finally, it is acknowledged that it would be desirable to test more hydrographs with low ξ values, as well as performing repeat runs, to determine both the range and consistency of unsteady flow conditions under which CCW hysteresis is observed.

5.1.3. Variability in Bed Load Yields and Effect of Sediment Grading

In river engineering, knowledge of the overall bed load sediment transport yield during a flood hydrograph event is particularly important in managed fluvial systems (e.g., downstream of a dam; Kondolf, 1997; Humphries et al., 2012), where deficient upstream sediment supply can deplete in-channel stored sediments, leading to bed degradation, channel incision, and widening processes. Within the current study, the influence of key hydrograph parameters (η, Γ_{HG}, and W_k) on bed load transport yields has, for the first time, been studied systematically for net degrading beds under zero sediment feed. For the range of hydrographs tested, it is apparent that total water work W_k (equation (2)) has the primary influence on bed load yields (i.e., Figure 4a) generated entirely through the depletion of in-channel stored sediments. By contrast, hydrograph unsteadiness Γ_{HG} (equation (1) and Figure 4b) and asymmetry η (equation (3)) appear to have secondary and negligible influences, respectively, on bed load yields. Regression analysis of bulk sediment yields W_t^* indicate strong correlation ($R^2 > 0.99$) with the combined hydrograph parameter ξ, in the form of a power law (equation (8)), which collapses satisfactorily with equivalent yield data obtained from Lee et al. (2004); see Figure 4c. Both the current study and Lee et al. (2004) were conducted with uniform coarse sand bed sediments and, as such, ξ does not account for potential grading effects from nonuniform sediments. In this context, Waters and Curran (2015) proposed a similar bed load yield model from their study of graded sand-gravel and sand-silt mixtures:

$$W_t^* = 22{,}762\chi^{1.072}, \tag{12}$$

where $\chi = W_k \, \Gamma_{\mathrm{HG}} \, (H_p/d_{50})$ combines the influence of hydrograph unsteadiness and total water work but also includes a length scale ratio (H_p/d_{50}) to account for different sediment grading. This χ parameter suggests implicitly that W_k and Γ_{HG} have equal influence on the sediment yields generated, whereas results from the current study indicate otherwise. This anomaly is highlighted by comparing the W_t^* values for benchmark hydrographs (i.e., U1a → U2a → U3a, Table 1) for which $\chi = 2.0$ in each case. (Note: $H_p/d_{50} \approx 60$ in all three hydrographs, while H_p is also included through Γ_{HG} [equation (1)], where $\Delta H = H_p - H_b$). As such, the expectation from equation (12) is that W_t^* should remain constant for these hydrographs, which is clearly not the case ($W_t^* = 5.52 \to 2.86 \to 1.62$ ($\times 10^4$), Table 1). Consequently, when this χ model is tested against a wider range of uniform and graded bed load yield data (e.g., Lee et al., 2004; Bombar et al., 2011; Wang et al., 2015), the overall level of fit is poor (Figure 9a). Indeed, the best fit regression relationship $W_t^* = 8157\chi^{1.202}$ to this expanded data set also demonstrates relatively poor correlation ($R^2 = 0.37$), again due largely to the equal weighting of W_k and Γ_{HG} in equation (12). It is therefore hypothesized that combining ξ with H_p/d_{50} may provide an improved bed load yield model for a wider range of sediments and hydrograph flow conditions, based on a similar power law form:

$$W_t^* = a\chi_m^b, \tag{13}$$

where a and b are proportionality coefficients and χ_m is a modified hydrograph-sediment parameter, written in the general form:
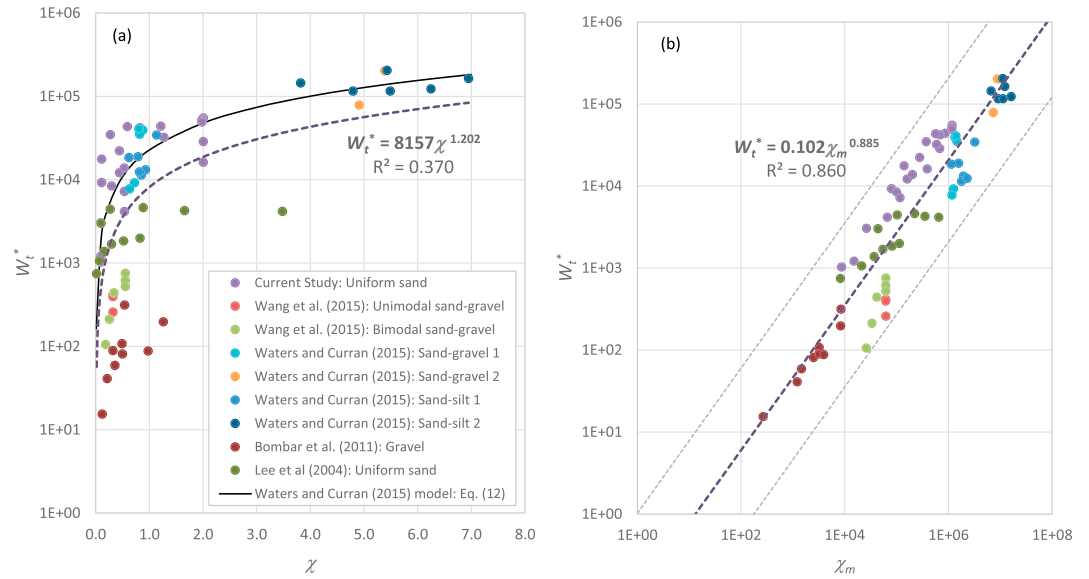
Figure 9. Variation in normalized bed load yield W_t^* with (a) $\chi = W_k \, \Gamma_{HG} \, (H_p/d_{50})$ and (b) $\chi_m = \xi \, (H_p/d_{50})^{2.5}$ (equation (14)). (Note: dashed black lines indicate best fit regression to all data sets; gray dashed lines in (b) show ± 1 order of magnitude in equation (15) predictions). Sediment yield model from Waters and Curran (2015) shown in (a) for comparative purposes.

$$\chi_m = \xi \left(H_p / d_{50} \right)^n. \tag{14}$$

Here, $n = 2.5$ is an empirical coefficient determined by best fit regression to relevant sediment yield data generated under different hydrographs. Figure 9b and equation (14) below thus present a new sediment yield model that is applicable to both uniform and graded sediments:

$$W_t^* = 0.102 \chi_m^{0.885}, \left(R^2 = 0.86 \right). \tag{15}$$

Sediment yield predictions from equation (15) lie within one order of magnitude (Figure 9b) of individual data sets with a wide range of (i) unsteady flows (triangular/trapezoidal hydrographs, Lee et al., 2004; Bombar et al., 2011; stepped hydrographs, Waters & Curran, 2015; smooth, continuous hydrographs, Wang et al., 2015; current study); (ii) sediment gradings (uniform coarse sands, Lee et al., 2004; current study; sand-silt mixtures, Waters & Curran, 2015; sand-gravel mixtures, Waters & Curran, 2015; Wang et al., 2015; gravel mixtures, Bombar et al., 2011); and (iii) upstream sediment supply conditions (zero sediment feed, Lee et al., 2004; Bombar et al., 2011; Wang et al., 2015; current study; recirculating sediments, Waters & Curran, 2015). It is therefore anticipated that this new empirical yield relationship can provide preliminary estimates of the sediment quantities transported from net degradational river reaches during hydrograph flood events for a wide range of unsteady flow and bed sediment conditions. As this model is derived solely from zero sediment feed or sediment starved/recirculated tests, it should be used with caution for the prediction of bed load yields under nonzero sediment supply conditions. In this context, Phillips et al. (2018) demonstrate that when input and output sediment fluxes are matched over a given hydrograph, sediment yields and transport hysteresis patterns do not vary systematically with hydrograph duration, shape, or flow magnitude, with these parameters relevant only through their contribution to the integrated transport capacity or total flow impulse. In many respects, however, this reflects the findings in the current study, where total water work W_k also represents an integrated flow property (i.e., total water volume) over the hydrograph duration, which is shown to have a primary control on sediment yield (Figure 4a) irrespective of hydrograph shape, flow magnitude, and duration. Our findings also indicate that hydrograph unsteadiness Γ_{HG} and asymmetry η, which are more representative of the rate of change in flow conditions over the hydrograph have, at best, a secondary influence on the overall sediment yields generated.

5.2. Morphological Response to Hydrographs and Zero Sediment Supply

5.2.1. Net Channel Degradation

Many alluvial channels considered to be in dynamic equilibrium can be destabilized readily by natural and human disturbances to flow and sediment regimes (Rinaldi & Simon, 1998; Simon & Rinaldi, 2006; Williams & Wolman, 1984), such as through controlled flow discharges (e.g., hydropower releases) and the decrease or cessation of upstream sediment supply (e.g., dam closure) in regulated rivers. Previous models to predict river bed degradation in managed fluvial systems are based largely on (i) predictions of sediment transport rates, more applicable under steady flow conditions (Hales et al., 1970; Jain & Park, 1989; Lu & Shen, 1986; Tinney, 1962), and (ii) temporal correlation of bed-level changes at surveyed channel profiles or cross sections (Rinaldi & Simon, 1998; Simon & Rinaldi, 2006; Wong & Parker, 2006). The latter approach is often used to describe nonlinear temporal changes in channel degradation patterns, with rapid initial degradation typically reducing asymptotically over longer time scales, either as hyperbolic (Williams & Wolman, 1984) or exponential (Simon, 1992) functions. Wong and Parker (2006) introduced the concept of an inlet "boundary layer" to define the short upstream transition region in which bed elevations and slopes were influenced primarily by specified unsteady flow conditions (triangular hydrographs). Downstream of this transition region, the bed elevations and slopes were found to be relatively unaffected by these unsteady flow conditions. Jain and Park (1989) derived a simplified functional relationship to predict spatial variability in river bed degradation downstream of a dam through combined numerical modeling and multiple regression analysis. This type of bed degradation under zero sediment feed conditions is also reported at several dam sites in Williams and Wolman (1984), with channel bed profiles typically remaining approximately parallel to the initial bed slope.

In the current study, the combined influence of zero sediment feed and the variable transporting capacity of individual flow hydrographs is shown to cause general bed degradation, with bed load transport yields W_t^* generated solely from depletion of in-channel stored bed sediments. Consequently, the initial channel incision depths Δz_0^* are found to correlate closely with W_t^* and the combined hydrograph parameter ξ through equations (8) and (10) (see Figure 6d). In addition, the asymptotic adjustment of final degraded bed elevations and bed slopes with downstream distance (Figures 6a–6c) is found to be well represented by an exponential function of normalized bed elevation $\Delta z^*(x)/\Delta z_0^*$ (Jain & Park, 1989) and downstream distance $x^* = x/L$ (Parker et al., 2007; see section S4 in the supporting information for details). This exponential model is generally applicable for all hydrographs resulting in net degradation along the full length of the erodible test bed section (i.e., for $\xi \geq 10$, Figure S4) and therefore provides insight into potential morphodynamic evolution (i.e., channel incision/bed degradation) in regulated rivers subject to hydrograph flows and limited sediment supply.

5.2.2. Generation of Bedforms

Bedforms also develop as a fundamental instability response to perturbations in the spatial and temporal scales of flow and sediment transport processes [e.g., Tubino, 1991; Eekhout et al., 2013; Martin & Jerolmack, 2013; Redolfi et al., 2018]. This is again highly pertinent in regulated rivers where unsteady flows are generated through controlled dam releases, natural flood events, or for managed stream restoration (Venditti et al., 2012). The response of bed morphology to unsteady flows also depends on upstream sediment supply and the availability, and relative mobility, of in-channel stored sediments. This presents inherent complexities in determining how evolving bedforms respond under different flow and sediment boundary conditions and whether these bedforms (can) approach stable, equilibrium dimensions (Tubino, 1991).

The current study focuses on the bed surface deformations, generated under different flow hydrographs and zero sediment feed conditions, which are shown to vary significantly depending on the relationship between the combined hydrograph parameter ξ and the bed load yields W_t^* generated (equation (8)). These bed surface measurements indicate that well-defined alternate bars (Figures 7a and 7b) form under hydrographs with the highest ξ values (and, hence, the largest bed load transport yields). By contrast, well-defined, regular dunes (Figure 7d) are shown to form under hydrographs with the lowest ξ values (and, thus, the smallest bed load yields). In the analysis of these different bedforms and their formative hydraulic conditions, it is important to consider the crucial role played by the channel width-to-depth ratio β. Under steady flow conditions, Colombini et al. (1987) defined a critical width-to-depth ratio β_c dependent on the Shields τ_b^* and relative roughness $\overline{d}_s = d_{50}/H$ parameters for the formation of equilibrium alternate bars, and below which (i.e., β
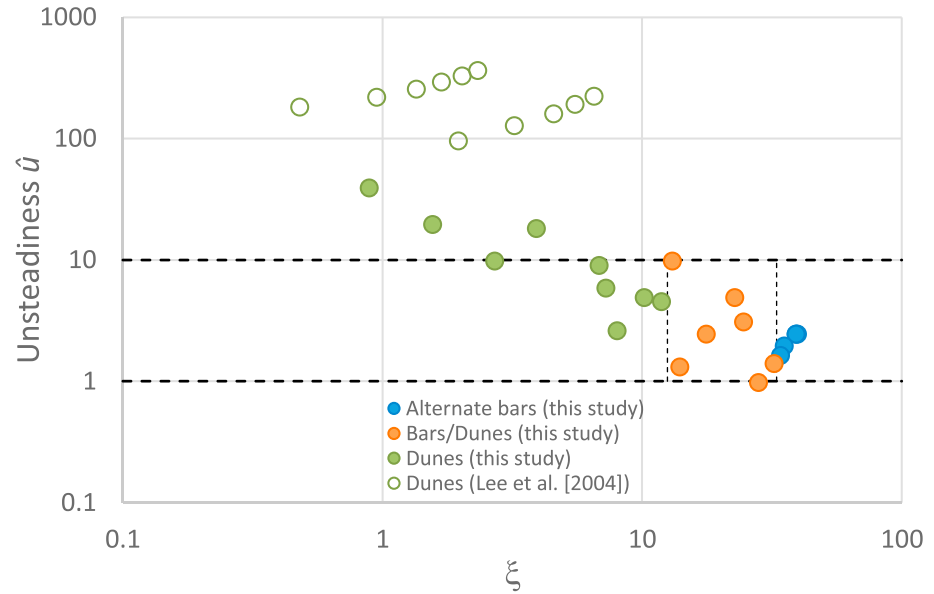
Figure 10. Regime plot of $\hat{u}$ versus ξ indicating the formative conditions for different bed forms generated under the hydrographs tested in the current study and Lee et al. (2004).

$< \beta_c$) bar formation was suppressed. In the current unsteady flow study, increasing discharges during the hydrograph rising limbs will increase β_c through an increase in τ_b^* and reduction in $\bar{d}_s$ (see Figure S5a; section S5 in the supporting information), while the actual width-to-depth ratio β in the channel will reduce due to increasing flow depth. As such, the potential for $\beta < \beta_c$ can be demonstrated for run U1a, within which well-defined alternate bars are shown to form (Figure 7a and Table 2). At base flow conditions, the $\beta = B/2H_b = 6.47$ is significantly higher than $\beta_c \approx 2.3$ (estimated from Figure S5a), whereas at the peak flow conditions, $\beta = B/2H_p = 3.13$ is considerably lower than $\beta_c \approx 8.0$. This suggests that bar development should be suppressed during high flow periods ($\beta < \beta_c$) in the hydrographs, based on the steady flow, "equilibrium amplitude" bar analysis by Colombini et al. (1987). It is clear, however, that well-defined alternate bars and more transitional bar/dune arrangements (Figure 7c) generated in the current study are not in equilibrium at any point due to unsteady hydrograph flow and zero sediment supply boundary conditions. The implications of the latter boundary condition in particular, which can result in significant depletion of in-channel stored bed sediments, clearly add significant complexity to any discharge dependence within bedforms generated under time-varying β and β_c values. This complexity may also be reflected in the observed variability in measured bedform geometry (i.e., wavelengths λ_{bf} and heights h_{bf}) generated in the deformed beds, as well as the significant irregularities in λ_{bf} and h_{bf} values between different hydrographs (see Table 2).

The formative conditions for alternate bars in unsteady flows can be predicted through application of an existing theoretical model by Tubino (1991; see section S5 in the supporting information for details). This model has been widely reported (e.g., Eekhout et al., 2013; Welford, 1993; Welford, 1994) to predict the occurrence of alternate bars in field studies, but, until now, has not been applied to zero sediment feed scenarios. In Tubino's (1991) model, the formative conditions for bar development are defined primarily by a parameter $\hat{u}$ (equation S5 and section S5), representing the time scale ratio between flow unsteadiness $\hat{\sigma}$ (equation S6, i.e., different from unsteadiness parameter Γ_{HG}) and morphology instability. The final bed configuration is thus strongly dependent on the magnitude of $\hat{u}$, such that when (i) $\hat{u} \sim O(1)$, bar development (and geometry) are influenced by flow unsteadiness $\hat{\sigma}$; (ii) $\hat{u} \gg 1$, bar development occurs over a much longer time scale than that associated with flow unsteadiness $\hat{\sigma}$; and (iii) $\hat{u} \ll 1$, bars develop on a much shorter time scale than that associated with flow unsteadiness $\hat{\sigma}$. Predicted $\hat{u}$ values in the current tests (Table 2) indicate that well-defined alternate bars (Figures 7a and 7b) and mixed bar/dune structures (Figure 7c) develop over similar time scales to flow unsteadiness $\hat{\sigma}$ (i.e., $\hat{u} = 1.63$–2.45 and 0.98–9.80, respectively [Table 2]; $\hat{u} \sim O(1)$).

These bar structures are also shown to develop under hydrographs with higher ξ values that induce larger overall bed load transport yields. Conversely, more regular dunes (Figure 7d) tend to develop either when bed load yields are much lower (i.e., for hydrographs with lower ξ values) or when time scales for bar development are significantly longer than those associated with flow unsteadiness $\hat{\sigma}$ (i.e., $\hat{u} = 2.61$–39.2 [Table 2]; $\hat{u} = O(1)$, and $\hat{u} \gg 1$, respectively). It is worth noting that the regular dunes reported in Lee et al. (2004) were also generated for predicted $\hat{u} \gg 1$ (i.e., $\hat{u} = 95.8$–364.8, Table 2).

A regime plot of the different bedform types is plotted in Figure 10 in $\hat{u}$:ξ space. This indicates that Tubino's (1991) model (i.e., through $\hat{u}$) predicts reasonably well the formative conditions for alternate bars, mixed dunes/bars, and regular dunes over the range of hydrographs tested under zero sediment feed. The plot also demonstrates that the combined hydrograph parameter ξ has a strong influence on the bedforms generated. This essentially confirms the intrinsic links between unsteady flow characteristics (i.e., through ξ), sediment yields (equation (8)) and in-channel bed degradation (equation (10)) as having a primary role in determining the overall bedform geometry that develops along the affected reach under zero feed conditions. Results from the current study also suggest that the time scales for bed morphology instability are always greater than those associated with flow unsteadiness (i.e., $\hat{u} > 1$, Figure 10), indicating that the nonequilibrium bedforms that develop are determined largely by the temporal lag in the morphological response to unsteady hydrograph flows.

6. Conclusions

A laboratory flume study is conducted to determine the influence of hydrograph flows on bed load sediment transport and associated changes to bed surface morphology under imposed zero sediment feed at the upstream boundary. The absence of sediment supply means that bed load transport rates and yields under different hydrographs are generated entirely from the degradation of in-channel stored bed sediments along the test section of the flume. These conditions are representative of flow-sediment-morphology scenarios typically encountered in regulated river reaches immediately downstream of a dam or reservoir impoundment. Three hydrograph parameters describing quantitatively the shape or asymmetry η, unsteadiness Γ_{HG}, and total water work W_k are varied systematically to determine their individual and collective influence on bed load transport characteristics and the morphodynamic response of a uniform, coarse sand bed under zero feed conditions.

Bed load transport rates measured over individual hydrographs demonstrate no consistent temporal lag between the peak sediment transport $q_{b,\max}$ and peak flow rates Q_p, with a degree of bed load plateauing observed around the peak flow region where the flow rate of change dQ/dt is reduced. The peak transport rates $q_{b,\max}$ are also shown to increase systematically with increasing Γ_{HG} and W_k (and reducing η) values. Corresponding phase plots highlight different transport hysteresis patterns depending on these flow hydrograph properties (η, Γ_{HG}, and W_k). CW or mixed/no (M/N) hysteresis are typically observed for hydrographs with higher W_k and lower Γ_{HG} values, while CCW hysteresis is limited to a few hydrographs with the lowest W_k and highest Γ_{HG} values. Variability in bed load hysteresis is also reflected by sediment yield ratios ψ during the rising and falling limbs, where CW and CCW hysteresis correspond universally to runs with $\psi > 1$ and $\psi < 1$, respectively, and M/N hysteresis is typically obtained for $\psi \geq 1$. The transition between $\psi < 1$ and $\psi > 1$ is shown to be relatively abrupt around a critical value of ratio W_k/Γ_{HG} and is well represented by a Boltzmann-type function.

A new hydrograph parameter ξ is defined to account for the combined influence of W_k and Γ_{HG} on bed load transport characteristics. In relation to bed load hysteresis, hydrographs with high, intermediate, and low ξ values are generally associated with CW, M/N, and CCW hysteresis patterns, respectively. Overall bed load yields W_t^* also display strong correlation ($R^2 > 0.99$) with ξ, providing a new empirical yield model for the hydrograph flows, zero sediment supply, and uniform bed sediment conditions considered in the current study and comparable prior studies (e.g., Lee et al., 2004). The influence of sediment grading on bed load yields is also considered through a modified hydrograph-sediment descriptor $\chi_m = \xi \cdot (H_p/d_{50})^{2.5}$, based on regression analysis to a wider range of data for both uniform and graded bed sediments. The resulting empirical power relationship between W_t^* and χ_m again provide good overall fit to these independent data sets ($R^2 = 0.86$).

The intrinsic link between hydrograph flows, sediment transport, and bed surface morphology is demonstrated by the three-way interaction between the sediment yield W_t^*, hydrograph parameter ξ, and the channel incision depth (i.e., bed degradation) along the channel. Different bedform arrangements (i.e., alternate bars, mixed bars/dunes, and regular dunes) also develop under different ranges of ξ values, although all remain in nonequilibrium due to the transient flow conditions and progressive bed degradation under zero sediment supply, reflected by the observed variability in bedform geometries. Analysis is therefore focused on their formative conditions by applying an existing theoretical model by Tubino (1991). Within this model, the formation of alternate bars is largely dependent on a parameter $\hat{u}$ representing the time scale ratio between flow unsteadiness and morphology instability. As such, within the current study, well-defined alternate bars or mixed bars/dunes form when $\hat{u} = O(1)$, while regular dunes often form when $\hat{u} \gg 1$, both as expected. Importantly, the zero sediment supply condition is also shown to control bedform geometry with well-defined, large-scale alternate bars developing under hydrographs with the highest ξ values and, hence, the largest in-channel sediment yields. By contrast, smaller-scale, regular dunes tend to develop under hydrographs with the lowest ξ values and, hence, the smallest in-channel sediment yields.

Results from the current study provide a systematic basis on which to develop new and improved model capabilities for the assessment of bed load sediment transport and morphodynamic response in regulated river reaches under hydrograph flows generated by natural flood events or managed dam releases and with no upstream sediment supply. Further work is also required to consider equivalent systematic bed load transport and morphology responses in managed river reaches when nonzero sediment influxes are either restricted or matched to output sediment fluxes.

References

Allen, J. R. (2009). River bedforms: Progress and problems. In J. D. Collinson & J. Lewin (Eds.), *Modern and Ancient Fluvial Systems*. https://doi.org/10.1002/9781444303773.ch2

Berta, A. M., & Bianco, G. (2010). An expression for the water-sediment moving layer in unsteady flows valid for open channels and embankments. *Natural Hazards and Earth System Sciences*, *10*(5), 1051–1059. https://doi.org/10.5194/nhess-10-1051-2010

Bombar, G., Elçi, Ş., Tayfur, G., Güney, M. Ş., & Bor, A. (2011). Experimental and numerical investigation of bed-load transport under unsteady flows. *Journal of Hydraulic Engineering*, *137*(10), 1276–1282. https://doi.org/10.1061/(ASCE)HY.1943-7900.0000412

Brakenridge, G. R. (2016), Global active archive of large flood events, Dartmouth Flood Observatory, University of Colorado, http://floodobservatory.colorado.edu/Archives/index.html.

Carling, P. A. (1999). Subaqueous gravel dunes. *Journal of Sedimentary Research*, *69*(3), 534–545. https://doi.org/10.2110/jsr.69.534

Church, M. (2006). Bed material transport and the morphology of alluvial river channels. *Annual Review of Earth and Planetary Sciences*, *34*(1), 325–354. https://doi.org/10.1146/annurev.earth.33.092203.122721

Colombini, M., Seminara, G., & Turbino, M. (1987). Finite amplitude alternate bars. *Journal of Fluid Mechanics*, *181*(1), 213–232. https://doi.org/10.1017/S0022112087002064

De Sutter, R., Verhoeven, R., & Krein, A. (2001). Simulation of sediment transport during flood events: Laboratory work and field experiments. *Hydrological Sciences Journal*, *46*(4), 599–610. https://doi.org/10.1080/02626660109492853

Eekhout, J., Hoitink, A., & Mosselman, E. (2013). Field experiment on alternate bar development in a straight sand-bed stream. *Water Resources Research*, *49*, 8357–8369. https://doi.org/10.1002/2013WR014259

Einstein, H. A. (1942). Formulas for the transportation of bed load. *Transactions of the American Society of Civil Engineers*, *107*(1), 561–577.

Graf, W. H., & Qu, Z. (2004). Flood hydrographs in open channels. *Proceedings of the institution of civil engineers-Water management*, *157*(1), 45–52. https://doi.org/10.1680/wama.2004.157.1.45

Graf, W. H., and L. Suszka (1985), Unsteady flow and its effect on sediment transport, in Proc. 21st IAHR Congress, edited, pp. 1-5, Melbourne, Australia.

Gunsolus, E. H., & Binns, A. D. (2017). Effect of morphologic and hydraulic factors on hysteresis of sediment transport rates in alluvial streams. *River Research and Applications*, *34*, 183–192.

Hales, Z. L., Shindala, A., & Denson, K. H. (1970). Riverbed degradation prediction. *Water Resources Research*, *6*(2), 549–556. https://doi.org/10.1029/WR006i002p00549

Hassan, M. A., Roey, E., & Parker, G. (2006). Experiments on the effect of hydrograph characteristics on vertical grain sorting in gravel bed rivers. *Water Resources Research*, *42*, W09408. https://doi.org/10.1029/2005WR004707

Humphries, R., Venditti, J. G., Sklar, L. S., & Wooster, J. K. (2012). Experimental evidence for the effect of hydrographs on sediment pulse dynamics in gravel-bedded rivers. *Water Resources Research*, *48*, W01533. https://doi.org/10.1029/2011WR010419

Jain, S. C., & Park, I. (1989). Guide for estimating riverbed degradation. *Journal of Hydraulic Engineering*, *115*(3), 356–366. https://doi.org/10.1061/(ASCE)0733-9429(1989)115:3(356)

Kondolf, G. M. (1997). Hungry water: Effects of dams and gravel mining on river channels. *Environmental management*, *21*(4), 533–551. https://doi.org/10.1007/s002679900048

Lee, K. T., Liu, Y. L., & Cheng, K. H. (2004). Experimental investigation of bedload transport processes under unsteady flow conditions. *Hydrological Processes*, *18*(13), 2439–2454. https://doi.org/10.1002/hyp.1473

Lu, J. Y., & Shen, H. W. (1986). Analysis and comparisons of degradation models. *Journal of Hydraulic Engineering*, *112*(4), 281–299. https://doi.org/10.1061/(ASCE)0733-9429(1986)112:4(281)

Mao, L. (2012). The effect of hydrographs on bed load transport and bed sediment spatial arrangement. *Journal of Geophysical Research*, *117*, F03024. https://doi.org/10.1029/2012JF002428

Mao, L., J. Cooper, and L. Frostick (2010), Hydrograph effects on sediment transport and surface grain sorting and organization, in Gravel-bed Rivers 7 Conference, edited, Tadoussac, Québec.

Martin, R. L., & Jerolmack, D. J. (2013). Origin of hysteresis in bed form response to unsteady flows. *Water Resources Research*, *49*, 1314–1333. https://doi.org/10.1002/wrcr.20093

Oh, J., & Tsai, C. W. (2010). A stochastic jump diffusion particle-tracking model (SJD-PTM) for sediment transport in open channel flows. *Water Resources Research*, *46*, W10508. https://doi.org/10.1029/2009WR008443

Parker, G. (1979). Hydraulic geometry of active gravel rivers. *Journal of the Hydraulics Division*, *105*(9), 1185–1201.

Parker, G., Hassan, M., & Wilcock, P. (2007). Adjustment of the bed surface size distribution of gravel-bed rivers in response to cycled hydrographs. *Developments in Earth Surface Processes*, *11*, 241–285. https://doi.org/10.1016/S0928-2025(07)11127-5

Parker, G., Klingeman, P. C., & McLean, D. G. (1982). Bedload and size distribution in paved gravel-bed streams. *Journal of the Hydraulics Division*, *108*(4), 544–571.

Pathirana, K., Ranasinghe, P., & Ratnayake, U. (2006). Bed shear stress in unsteady open channel flow over rough beds. *Journal of the Institution of Engineers*, *41*(01), 7–12.

Phillips, B. C., & Sutherland, A. J. (1990). Temporal lag effect in bed load sediment transport. *Journal of Hydraulic Research*, *28*(1), 5–23. https://doi.org/10.1080/00221689009499144

Phillips, C. B., Hill, K. M., Paola, C., Singer, M. B., & Jerolmack, D. J. (2018). Effect of flood hydrograph duration, magnitude, and shape on bed load transport dynamics. *Geophysical Research Letters*, *45*, 8264–8271. https://doi.org/10.1029/2018GL078976

Piedra, M. M. (2010), Flume investigation of the effects of sub-threshold rising flows on the entrainment of gravel beds, University of Glasgow.

Raudkivi, A. J. (1997). Ripples on stream bed. *Journal of Hydraulic Engineering*, *123*(1), 58–64. https://doi.org/10.1061/(ASCE)0733-9429(1997)123:1(58)

Redolfi, M., Bertoldi, W., Tubino, M., & Welber, M. (2018). Bed load variability and morphology of gravel bed rivers subject to unsteady flow: A laboratory investigation. *Water Resources Research*, *54*, 842–862. https://doi.org/10.1002/2017WR021143

Rinaldi, M., & Simon, A. (1998). Bed-level adjustments in the Arno River, central Italy. *Geomorphology*, *22*(1), 57–71. https://doi.org/10.1016/S0169-555X(97)00054-8

Rushmer, E. L. (2007). Physical-scale modelling of jökulhlaups (glacial outburst floods) with contrasting hydrograph shapes. *Earth Surface Processes and Landforms*, *32*(6), 954–963. https://doi.org/10.1002/esp.1461

Simon, A. (1992). Energy, time, and channel evolution in catastrophically disturbed fluvial systems. *Geomorphology*, *5*(3-5), 345–372. https://doi.org/10.1016/0169-555X(92)90013-E

Simon, A., & Rinaldi, M. (2006). Disturbance, stream incision, and channel evolution: The roles of excess transport capacity and boundary materials in controlling channel response. *Geomorphology*, *79*(3-4), 361–383. https://doi.org/10.1016/j.geomorph.2006.06.037

Suszka, U. L. (1987). Sediment transport at steady and unsteady flow a laboratory study, PhD thesis, EPFL.

Tinney, E. R. (1962). The process of channel degradation. *Journal of Geophysical Research*, *67*(4), 1475–1480. https://doi.org/10.1029/JZ067i004p01475

Tubino, M. (1991). Growth of alternate bars in unsteady flow. *Water Resources Research*, *27*(1), 37–52. https://doi.org/10.1029/90WR01699

Venditti, J., Nelson, P., Minear, J., Wooster, J., & Dietrich, W. (2012). Alternate bar response to sediment supply termination. *Journal of Geophysical Research*, *117*, F02039. https://doi.org/10.1029/2011JF002254

Wang, L., Cuthbertson, A., Pender, G., & Cao, Z. (2015). Experimental investigations of graded sediment transport under unsteady flow hydrographs. *International Journal of Sediment Research*, *30*, 306–320. https://doi.org/10.1016/j.ijsrc.2015.03.010

Waters, K. A., & Curran, J. C. (2015). Linking bed morphology changes of two sediment mixtures to sediment transport predictions in unsteady flows. *Water Resources Research*, *51*, 2724–2741. https://doi.org/10.1002/2014WR016083

Welford, M. R. (1993), A field evaluation of the formative conditions, wavelengths and heights of alternate bars in alluvial channels, University of Illinois at Urbana-Champaign.

Welford, M. R. (1994). A field test of Tubino's (1991) model of alternate bar formation. *Earth Surface Processes and Landforms*, *19*(4), 287–297. https://doi.org/10.1002/esp.3290190402

Wijbenga, J., and G. Klaassent (2009), Changes in bedform dimensions under unsteady flow conditions in a straight flume, Modern and Ancient Fluvial Systems: Special Publication 6 of the IAS, 35.

Williams, G. P. (1989). Sediment concentration versus water discharge during single hydrologic events in rivers. *Journal of Hydrology*, *111*(1-4), 89–106. https://doi.org/10.1016/0022-1694(89)90254-0

Williams, G. P., and M. G. Wolman (1984), Downstream effects of dams on alluvial rivers. USGS report 1286, doi: https://doi.org/10.3133/pp1286, 83 p.

Wong, M., & Parker, G. (2006). One-dimensional modeling of bed evolution in a gravel bed river subject to a cycled flood hydrograph. *Journal of Geophysical Research*, *111*, F03018. https://doi.org/10.1029/2006JF000478

Yalin, M. S. (1992). *River mechanics*. Oxford, U.K: Pergamon Press.

Yen, C. l., & Lee, K. T. (1995). Bed topography and sediment sorting in channel bend with unsteady flow. *Journal of Hydraulic Engineering*, *121*(8), 591–599. https://doi.org/10.1061/(ASCE)0733-9429(1995)121:8(591)